Structure of the Madden–Julian Oscillation in the Superparameterized CAM

JAMES J. BENEDICT AND DAVID A. RANDALL

Department of Atmospheric Science, Colorado State University, Fort Collins, Colorado

(Manuscript received 11 December 2008, in final form 10 June 2009)

ABSTRACT

The detailed dynamic and thermodynamic space–time structures of the Madden–Julian oscillation (MJO) as simulated by the superparameterized Community Atmosphere Model version 3.0 (SP-CAM) are analyzed. Superparameterization involves substituting conventional boundary layer, moist convection, and cloud parameterizations with a configuration of cloud-resolving models (CRMs) embedded in each general circulation model (GCM) grid cell. Unlike most GCMs that implement conventional parameterizations, the SP-CAM displays robust atmospheric variability on intraseasonal space and time (30–60 days) scales. The authors examine a 19-yr SP-CAM simulation based on the Atmospheric Model Intercomparison Project protocol, forced by prescribed sea surface temperatures. Overall, the space–time structures of MJO convective disturbances are very well represented in the SP-CAM. Compared to observations, the model produces a similar vertical progression of increased moisture, warmth, and heating from the boundary layer to the upper troposphere as deep convection matures. Additionally, important advective and convective processes in the SP-CAM compare favorably with those in observations. A deficiency of the SP-CAM is that simulated convective intensity organized on intraseasonal space–time scales is overestimated, particularly in the west Pacific. These simulated convective biases are likely due to several factors including unrealistic boundary layer interactions, a lack of weakening of the simulated disturbance over the Maritime Continent, and mean state differences.

1. Introduction

The Madden–Julian oscillation (MJO), an eastward-moving couplet of convectively active and suppressed atmospheric conditions in the Indian and west Pacific Ocean regions, is the leading mode of tropical variability on 30–60-day (intraseasonal) time scales. Since its discovery in the early 1970s (Madden and Julian 1971), a host of observational, theoretical, and modeling studies have gradually improved our understanding of the MJO but have also revealed its many complexities (e.g., Madden and Julian 2005; Zhang 2005). For example, we do not yet have adequate explanations of MJO convective initiation in the Indian Ocean, scale interactions linking individual cloud processes to planetary-scale waves, and the role of air–sea coupling. Because equatorial heating associated with organized convective systems such as the MJO has far-reaching impacts, an accurate representation of tropical variability in general circulation models (GCMs) is critical for producing realistic patterns of global weather and climate. Unfortunately, most current GCMs do not simulate the MJO well, lacking sufficient variability on intraseasonal space–time scales (Lin et al. 2006). This study investigates the physical structure of the MJO simulated by the so-called superparameterized Community Atmosphere Model (SP-CAM), a modified GCM that exhibits substantially more realistic intraseasonal variability.

The poor representation of the MJO is a well-documented deficiency plaguing many current GCMs (Slingo et al. 1996; Lin et al. 2006; Kim et al. 2009). Lin et al. (2006) present results from 14 coupled GCMs participating in the Intergovernmental Panel on Climate Change (IPCC) Fourth Assessment Report (AR4) and find that the magnitude of intraseasonal variability in 12 of those models was less than half of the observed value. Those authors conclude that improvements in the representation of subgrid-scale processes in the model (e.g., boundary layer and moist convective processes, saturated and unsaturated convective downdrafts, etc.) would lead to a more accurate MJO depiction.

Traditional GCMs have grid spacings of $O(100\ \text{km})$ and thus cannot accurately resolve subgrid-scale cloud

Corresponding author address: Jim Benedict, Department of Atmospheric Science, Colorado State University, Fort Collins, CO 80523–1371.
E-mail: jim@atmos.colostate.edu

DOI: 10.1175/2009JAS3030.1

and boundary layer processes without making some assumptions about how such processes ''behave.'' Parameterizations are semiempirical theories that predict the statistical behavior of subgrid-scale processes and their physical interactions with each other and with resolved-scale phenomena. A major weakness of parameterizations is that they artificially separate subgrid-scale processes that are highly interactive in nature. One approach to bypassing this limitation is to replace certain conventional parameterizations with cloud-resolving models (CRMs; Grabowski and Smolarkiewicz 1999; Grabowski 2001), a technique termed ''superparameterization'' (Khairoutdinov and Randall 2001). Replacing conventional cloud parameterizations with CRMs of horizontal resolution O(1 km) allows cloud-scale dynamics, moist processes, and radiation to interact in a more natural manner (Grabowski 2001). Specific conventional parameterizations, including radiation and microphysics, are still implemented in superparameterized models; however, because such parameterizations are inherently limited by their input conditions to begin with, improvement of the input conditions through superparameterization contributes to further improvement in the results (Randall et al. 2003). Although great progress has been made in using a global CRM to produce a single but realistic MJO (e.g., Miura et al. 2007), simulations of sufficient duration to analyze systematic MJO behavior—ideally, multiple years—remain computationally prohibitive (Khairoutdinov et al. 2008, hereafter KDR08). The method of superparameterization thus bridges the computational gap between conventionally parameterized GCMs and global CRMs.

The simulated data used in this study are taken from a superparameterized version of the National Center for Atmospheric Research (NCAR) Community Atmosphere Model version 3.0 (CAM3.0; Collins et al. 2006), called the SP-CAM. The SP-CAM simulation being analyzed is based on the Atmospheric Model Intercomparison Project (AMIP) protocol (Gates 1992) in that the model is forced by observed sea surface temperatures (SSTs). The current SP-CAM and previous versions of it demonstrate a remarkable increase in intraseasonal variability relative to the standard CAM (e.g., Randall et al. 2003). Using a suite of standardized diagnostics, Kim et al. (2009) find that the SP-CAM demonstrates good skill in representing the MJO relative to seven other GCMs, including versions of the CAM with updated parameterizations. Several explanations relating poor MJO depiction in the standard CAM and its intensified signal in superparameterized GCMs have been proposed recently. Thayer-Calder and Randall (2009) find that insufficient column moistening during convective development in CAM3.0 is related to the choice of deep convection parameterization. They conclude that this lack of moistening severely limits that model's intraseasonal variability. Zhu et al. (2009) compare CAM3.0 to the SP-CAM and discover that organized convection in the SP-CAM is delayed until a moister environment is achieved. The delayed initiation appears to result in an MJO wet phase with more vigorous convection, higher rain rates, and a stratiform heating profile that more closely resembles observations. Additionally, Luo and Stephens (2006), in their study of the Asian summer monsoon, postulate that convective enhancement in two superparameterized GCMs is related to an overly intense convection–wind–evaporation feedback augmented by the CRM's periodic boundary conditions. Our analysis provides additional insight of the MJO structure in the SP-CAM and proposes an explanation regarding its more realistic but overly intensified MJO convection.

Section 2 of this paper reviews the SP-CAM setup and describes the simulated and observation-based datasets. MJO event selection and compositing techniques are discussed in section 3. Results displaying the composite MJO space–time structure are presented in section 4, followed by a discussion and summary in section 5.

2. Data sources

a. AMIP run with the SP-CAM

The NCAR CAM3.0 (Collins et al. 2006) acted as the host GCM. CAM3.0 has a 2.8° × 2.8° horizontal grid (T42 spatial truncation), 30 levels up to 3.6 hPa, and a time step of 30 min. Embedded within each GCM grid cell is a 2D ''curtain'' of 32 CRM grid columns oriented in the north–south direction, with 4-km horizontal grid spacing, periodic boundary conditions, 28 levels collocated with the 28 lowest CAM levels, and a time step of 20 s. The 2D CRM replaces the CAM's conventional parameterizations of moist physics, convection, turbulence, and boundary layer processes. As discussed in Khairoutdinov et al. (2005), momentum feedback from the CRM to the GCM is not allowed. Coupling between the surface and atmosphere is computed only on the GCM grid such that enhanced, localized surface fluxes that may arise from gust fronts are not included. CRM-scale enhancements of surface drag related to localized gustiness of near-surface winds are explicitly included, however. Additional details of the SP-CAM AMIP simulation used in this study can be found in KDR08.

Figure 1 presents a simplified picture of the coupling between the host GCM and embedded CRMs. Further discussion of GCM–CRM coupling can be found in

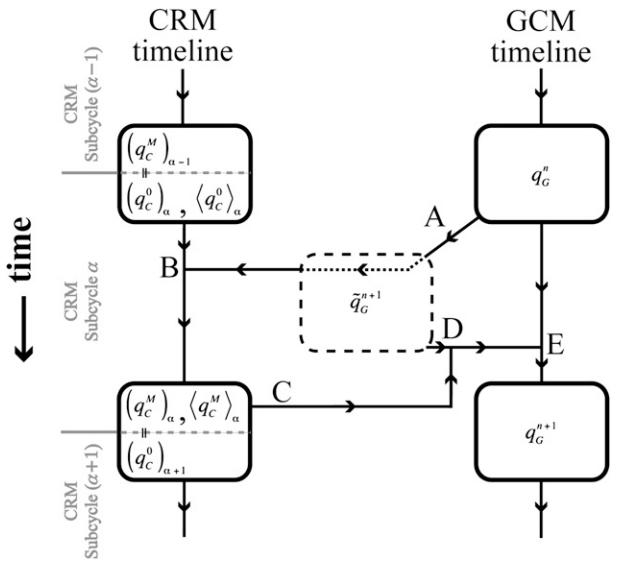

FIG. 1. Schematic diagram of the coupling between the GCM and CRM in superparameterized models. Time-stepping n to $n + 1$ in the GCM, a provisional value of a prognostic variable q is first computed using only non-CRM, large-scale advective tendencies (A). The CRM field q_c, initiated with the q field from the end of the previous CRM subcycle ($\alpha - 1$) such that continuous integration occurs in the CRM, is time-stepped through subcycle α with CRM advection, CRM physics, and a relaxation term (B). The relaxation term prevents drift of CRM field q_C from GCM field q_G and involves the CRM domain-averaged q field from the start of the subcycle, $\langle q_C^0 \rangle$, along with $\tilde{q}_G^{n+1}$. During subcycle α, the CRM is integrated from $m = 0$ to $m = M$ corresponding to GCM time steps n and $n + 1$, respectively. At the end of subcycle α, the CRM domain-averaged field $\langle q_C^M \rangle_\alpha = \langle q_C^{n+1} \rangle_\alpha$ (C) is combined with $\tilde{q}_G^{n+1}$ (D) and non-CRM, large-scale advective tendencies (E) to arrive at q_G^{n+1}. A discussion is given in the appendix.

Khairoutdinov and Randall (2003) and Khairoutdinov et al. (2005). In Fig. 1, q represents liquid water/ice moist static energy or total nonprecipitating water (i.e., it is a prognostic thermodynamic variable excluding total precipitating water). Mathematically, the CRM is influenced by the GCM through a relaxation term that prevents drift of the CRM fields away from those of the GCM; simultaneously, the CRM is forced by the GCM's large-scale advection. The GCM, in turn, is modified by CRM domain-averaged tendencies of temperature, water vapor, and nonprecipitating liquid arising from cloud processes on the CRM grid.

The AMIP simulation was conducted using prescribed monthly mean (interpolated to daily mean) SSTs and sea ice concentrations (Hurrell et al. 2008). The simulation produced 19 yr of global daily output spanning 1 September 1985 to 25 September 2004. Our analysis utilizes pentad-averaged SP-CAM fields interpolated to a 2.5° × 2.5° horizontal grid (see Table 1 for a summary of data sources).

b. Observations and reanalysis

We compare the SP-CAM AMIP simulation results to a host of observation-based datasets. The aim of this study is to examine a large sample of MJO events with particular focus on their mesoscale to planetary-scale spatial features. To maximize the number of events, we seek observation-based datasets with a sufficiently long temporal range (at least 14 yr) and minimal missing data points. Owing to this limitation, a pentad-averaged version of the 40-yr European Centre for Medium-Range Weather Forecasts (ECMWF) Re-Analysis (ERA-40; Uppala et al. 2005) is utilized as the observational basis for most dynamic and thermodynamic fields. ERA-40 has the advantage of complete data coverage in remote and data-sparse areas of the Indian and Pacific Oceans but is also subject to errors introduced by parameterizations, particularly in the boundary layer and aloft in highly convective situations (ECMWF 2003 and references therein). Despite the dependence of ERA-40 on parameterizations, previous studies suggest that the overall synoptic and mesoscale features associated with tropical intraseasonal disturbances in warm-ocean regions are well represented by ECMWF reanalyses (Lin and Johnson 1996; Straub and Kiladis 2003; Sperber 2003; Kiladis et al. 2005, hereafter KSH05).

We use 19 yr of pentad-averaged rain data from the Global Precipitation Climatology Project (GPCP). This version of pentad GPCP data is a companion dataset to the monthly GPCP archive (Adler et al. 2003), which merges rain gauge measurements with space-borne infrared and microwave retrievals on a 2.5° × 2.5° grid. Remotely sensed measurements of precipitable water are based on the National Aeronautics and Space Administration (NASA) Water Vapor Project (NVAP; Randel et al. 1996). NVAP blends radiosonde, infrared, and microwave measurements to produce a comprehensive global dataset spanning 14 yr (1 January 1988–31 December 2001). We use outgoing longwave radiation (OLR) measurements from the International Satellite Cloud Climatology Project (ISCCP; Zhang et al. 2004), and SSTs are taken from version 2 of the National Oceanic and Atmospheric Administration (NOAA) Optimal Interpolation SST (OISST2; Reynolds et al. 2002).

3. Methodology

Our approach to isolating and compositing MJO events is very similar to that described by Benedict and Randall (2007). Pentad GPCP rain is spectrally filtered to identify intraseasonal convective envelopes. Using the space–time coordinates of MJO-filtered convective activity, we then return to the unfiltered rain dataset to

TABLE 1. Primary data sources used in this study.

	SP-CAM	ERA-40	GPCP	NVAP	ISCCP
Origin/platform	Model	Radiosonde and satellite measurements, model forecasts	Satellite and rain gauge measurements	Satellite and radiosonde measurements	Satellite measurements
Horizontal resolution	2.5° × 2.5°[a]	2.5° × 2.5°	2.5° × 2.5°	2.5° × 2.5°[c]	2.5° × 2.5°
Temporal resolution and domain	Pentad;[b] 1 Sep 1985–25 Sep 2004	Pentad;[b] 1 Jan 1984–31 Dec 2001	Pentad; 1 Jan 1984–31 Dec 2001	Pentad;[b] 1 Jan 1988–31 Dec 2001	Pentad; 1 Jan 1984–31 Dec 2001
Vertical levels	30, 3.6 hPa top; 7 levels below 850 hPa	13; 1000, 925, 850, 775, 700, 600, 500, 400, 300, 250, 200, 150, 100 hPa	Surface	Column integration	Top of atmosphere
Selected variables	Dynamic and thermodynamic fields	Dynamic and thermodynamic fields	Total precipitation	Precipitable water	OLR

[a] Interpolated from 2.8° × 2.8° horizontal grid.
[b] 5-day averages calculated from daily data.
[c] Interpolated from 1° × 1° horizontal grid.

generate MJO event composites based on the longitude and pentad of maximum rain. In essence, we utilize spectrally filtered signals simply as a guide in our selection of intraseasonal convective events; the actual event selection and all subsequent analyses are based on unfiltered data. This procedure helps to maintain spatial and temporal fidelity of synoptic and mesoscale features that might be masked by the filtering process. Influences from high-frequency phenomena such as inertia–gravity waves are essentially eliminated through the use of pentad-averaged data. Evidence of mixed Rossby–gravity waves and tropical depressions may nevertheless arise in individual MJO events owing to the selection procedure. In a composite of numerous MJO events, however, such features will tend to be eliminated by averaging.

At the beginning of the event selection process, we subtract the mean and first three harmonics of the seasonal cycle from GPCP rainfall at each grid point. Following the methods of Wheeler and Kiladis (1999), we retain rain data only within the appropriate MJO spectral region (zonal wavenumbers +1 to +5, indicating eastward-propagating disturbances, and 20–100-day periods). A zonal wavenumber–frequency diagram of tropical rainfall indicates that the eastward component of intraseasonal planetary disturbances is substantial, whereas the corresponding westward counterpart is small for both the model and observations (not shown). Thus, the influence of westward components that are coherent with eastward components is small (Hayashi 1979) and our method of filtering will accurately capture eastward-propagating signals. The data are then averaged between 10°S and 5°N, corresponding to the latitude band of greatest MJO variability in boreal winter (Wheeler and Kiladis 1999). We scan the MJO-filtered, pentad- and meridionally averaged GPCP rain field to locate broad convective envelopes, labeling them ''events'' if they pass a specific set of criteria based on spatial extent, temporal duration, and rain intensity (Benedict and Randall 2007). Only events occurring within 50°E–170°W during boreal nonsummer months (15 September–31 May) are used. The time and longitude of maximum filtered rain for each MJO event are recorded. We return to the unfiltered, meridionally averaged version of GPCP rain and locate the recorded time and longitude. Often the time and longitude of rain maximum in the filtered field does not exactly match that of the unfiltered data, so we scan a small area (±1 pentad, ±15° longitude) in the unfiltered dataset to locate an updated temporal and spatial coordinate of rain maximum. This position in time t_o and space L^* of maximum rain in the unfiltered data field acts as the base point (day 0) upon which all other unfiltered variables are centered. With L^* fixed, we take a time series of any variable from 30 days prior to the most intense MJO-related rainfall ($t_o = -30$) to 20 days following it ($t_o = +20$). This time series essentially shows the temporal evolution, at L^*, of any unfiltered variable during an MJO event. By gathering the time series at all available pressure levels, we can generate time–height cross sections for any variable and any identified MJO event. We form a composite MJO by aligning the t_o values (lag day 0) of all events.

It is important to note that L^* can be located anywhere within the equatorial Indian and west Pacific sectors. Therefore, departures from the calendar-day

mean at L^* are used in the composite MJO cross sections (except where noted). One can think of this space–time anomaly as a departure from what would be expected at the time of year associated with t_o and at longitude L^*. This reduces the effects of the basic-state differences in which the MJO operates, such as the change in climatological 850-hPa zonal winds from westerly over the Indian Ocean to easterly over the International Date Line during boreal winter (Fig. 2r). An identical MJO event selection and compositing procedure is also applied to the SP-CAM data.

4. Results

a. Boreal winter-mean state

Several studies have highlighted the seasonal mean differences between CAM3.0 and a number of SP-CAM simulations (Khairoutdinov et al. 2005; KDR08). Examining the climatological background in which the MJO operates provides an understanding of some of the fundamental relationships between moisture, clouds, and convection on space–time scales larger than the MJO itself. Knowledge of climatological biases is also important regarding the interpretation of the composite anomaly plots shown later in this section.

November–March means and corresponding model biases based on all available years are displayed for selected variables in Fig. 2 (see Table 1 for dataset temporal ranges). Longitudinal cross sections of model biases averaged from 10°S to 5°N are shown along the bottom row of Fig. 2. A comparison of total rainfall between the SP-CAM and GPCP observations (Fig. 2c) indicates simulated wet biases over the western Indian Ocean, the waters north of Australia, and the west Pacific. A dry bias is noted over Maritime Continent landmasses and the extreme eastern Indian Ocean. We can infer from biases in OLR (Fig. 2g) that simulated boreal winter deep convection and associated cirrus clouds are unrealistically widespread in the west Pacific warm pool region but lacking in coverage over the western Maritime Continent and eastern Indian Ocean.

Across a broad area of the Maritime Continent, simulated mean precipitable water (PW) values (Fig. 2k) are lower than observed climatology. The largest PW difference is collocated with the simulated dry rainfall and positive OLR biases. Weakly positive biases in SP-CAM PW appear in the extreme western Indian Ocean and near the International Date Line. Figure 2o presents a dry bias pattern of simulated specific humidity at 600 hPa (q_{600}) that is similar to that of PW. The equatorial band of maximum q_{600} in the model is unrealistically dry and narrow over the western Maritime Continent compared to observations (Fig. 2n), while biases are nearly zero across much of the Indian and Pacific sectors. The SP-CAM also underestimates boundary layer moisture over landmasses of the Maritime Continent (by 10% of climatology), northern Australia (20%), and southeast Asia (25%; not shown). Mirroring these dry biases in the SP-CAM, strong negative θ_e biases at 600 and 925 hPa over Maritime Continent landmasses are also apparent (not shown). Away from the Maritime Continent region, no substantial biases are observed in any of the thermodynamic variables discussed above.

In eastern Indonesia and the west Pacific, the SP-CAM exhibits a tendency for unrealistically strong low-level west winds but a nearly zero wind bias at upper levels (Figs. 2t and 2x, respectively). In the Indian Ocean sector, simulated climatological low-level westerlies and upper-level easterlies are too weak compared to ERA-40. Together, Figs. 2q–x suggest greater speed convergence (divergence) of the simulated climatological zonal winds in the upper (lower) troposphere over the western Maritime Continent. Additionally, more intense low-level simulated zonal convergence in the west Pacific can be inferred from a comparison of Figs. 2q and 2r. These inferences agree nicely with bias plots of rainfall (Fig. 2d), OLR (Fig. 2h), and PW (Fig. 2l), indicating that climatological deep convection in the SP-CAM is overestimated in the west Pacific and underestimated in western Indonesia and the eastern Indian Ocean. The biases in Fig. 2 appear to resemble the phase of the MJO when convection is enhanced over the west Pacific and suppressed over the eastern Indian Ocean. Analysis of identified MJO disturbances indicates that simulated events in the region of the dry climatological bias (90°–110°E) have slightly weaker convection than observed events, a deficiency also found in coupled simulations (Zhang et al. 2006). Given that the MJO is one of the larger contributors to boreal winter deep convection in the west Pacific (Wheeler and Kiladis 1999), the longitudinal bias profiles suggest that MJO-related convection in the west Pacific region might be unrealistically vigorous in the SP-CAM. As we will illustrate shortly, this is indeed the case.

b. MJO events

We identified 46 MJO events in the GPCP dataset and 50 in the SP-CAM dataset. A summary of the temporal and spatial event locations is displayed in Fig. 3. This plot indicates the time t_o and longitude L^* (organized into monthly and 10° wide bins, respectively) at which each identified MJO event was most intense as measured by surface rainfall rate. Events based on observed precipitation (Fig. 3a) tend to have their maximum intensities clustered in two areas: the east Indian Ocean from November to January and the west Pacific Ocean

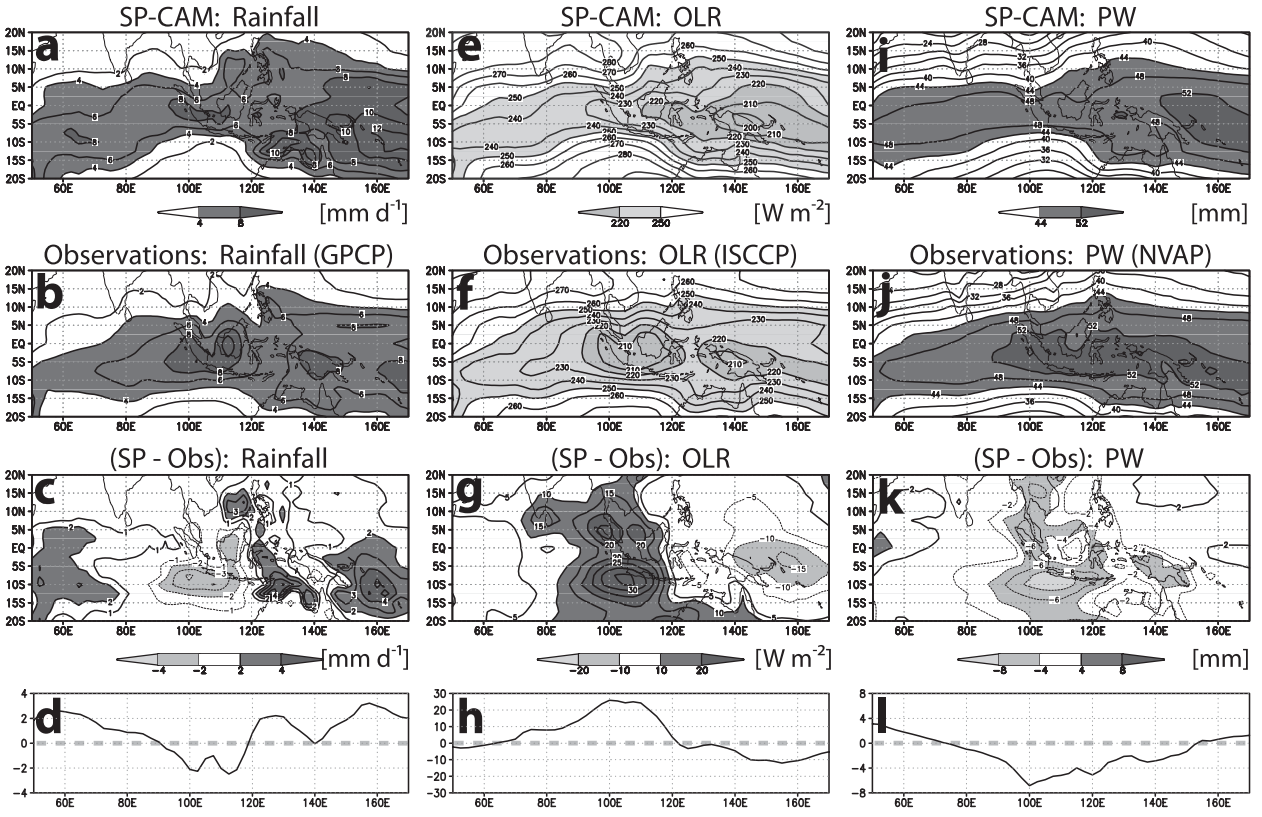

FIG. 2. November–March mean fields of total rainfall, OLR, precipitable water, 600-hPa specific humidity (q_{600}), 850-hPa zonal wind (u_{850}), and 200-hPa zonal wind (u_{200}) based on all available years (see Table 1 for data temporal ranges). Mean fields corresponding to the SP-CAM, observations, their difference (SP-CAM − observations), and the meridional average (10°S–5°N) of their difference are displayed from top to bottom.

during boreal spring. To a lesser extent, there is also a cluster of events in the east-central Indian Ocean in April and May possibly tied to Asian monsoon activity (Jones et al. 2004).

It is less common for MJO events in nature to have their maximum intensity over the Maritime Continent between 110° and 140°E (Fig. 3a). In this region, the effects of an enhanced diurnal cycle and a disruption of low-level winds and surface heat fluxes by the terrain can weaken intraseasonal variability (e.g., Inness and Slingo 2006 and references therein). Events are often strongest during December with a secondary maximum in May. In the model (Fig. 3b), MJO events occur most frequently in December with a secondary maximum in May, mirroring nature. Unlike observations, however, simulated events have peak intensities most frequently over the Maritime Continent (120°–130°E) rather than over the east Indian Ocean (although overall composite rainfall is greater for west Pacific events). This is consistent with Fig. 2c and with the finding by Khairoutdinov et al. 2005 that boreal winter rainfall over eastern Indonesia and northern Australia, a sizable portion of which is related to MJO activity, is substantially overestimated by the SP-CAM. The weaker secondary peak of simulated MJO disturbances occurs near 150°–160°E and matches observations. There is an overall weaker event clustering in the model, with only a broad maximum over the Maritime Continent between December and May and a second isolated peak at the International Date Line in December.

c. *Time–height structure of basic variables*

Observed time–height structures of the MJO life cycle have become increasingly well documented in recent years (e.g., Woolnough et al. 2000; Kemball-Cook and Weare 2001; Sperber 2003; Myers and Waliser 2003; KSH05; Benedict and Randall 2007). Figure 4 displays composite MJO life cycles of several variables. Composites are based on all identified MJO events. In all figures, time is plotted from right to left to mimic a zonal cross section such that negative lag days correspond to positions east of deep convection. Composited total rainfall from GPCP, SP-CAM, and their difference (Fig. 4d, repeated in Fig. 4h) is also displayed.

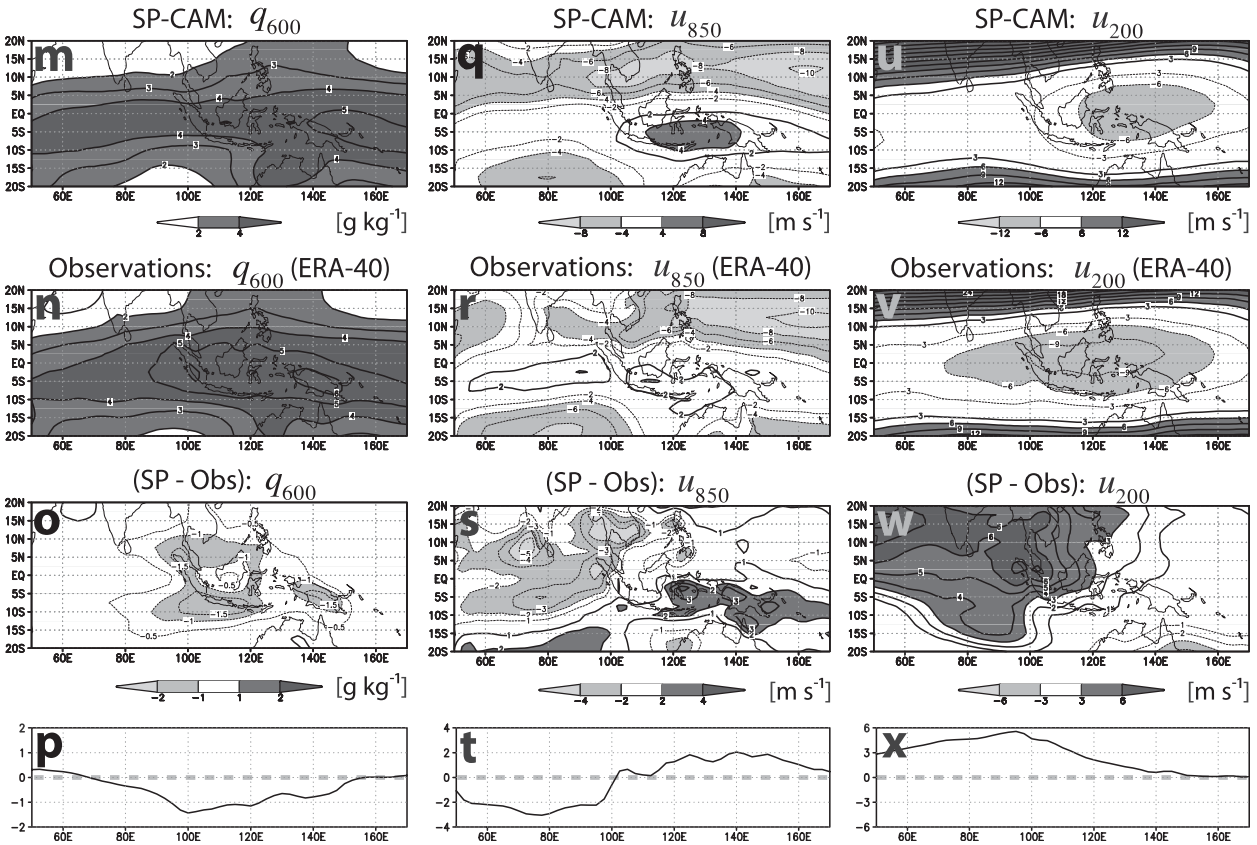

FIG. 2. (*Continued*)

A comparison of zonal wind anomalies in ERA-40 and SP-CAM (Figs. 4a and 4e, respectively) suggests that the SP-CAM results closely match the qualitative structural evolution of the MJO passage despite some differences in the magnitude of certain features. Specifically, the general baroclinic structure, the timing and vertical structure of westerly onset, and the timing and magnitude of maximum westerlies following deep convection are well simulated by the model. The simulated magnitude and temporal extent of low-level easterly and upper-level westerly anomalies prior to maximum rainfall appear to be too large, however, suggesting an overly intensified transient Walker-type circulation in the SP-CAM. KSH05 used data from several radiosonde stations to show that the development of significant low-level easterly winds prior to MJO deep convection tended to occur around day −25, slightly earlier than the ERA-40 results might suggest and closer in line with the SP-CAM cross section.

Composite moisture profiles (Figs. 4b and 4f) indicate moistening of the initially dry free troposphere, first in the lower levels and then deepening to the upper levels as convection intensifies. This feature is seen in both ERA-40 and SP-CAM, as are day-0 q' maxima at 650 hPa and drying following maximum rainfall. Whereas reanalysis has distinct dry periods throughout the entire troposphere before and after heaviest rains, the q' evolution in the model is shifted positively such that dry periods are less dry and wet periods are wetter. This discrepancy is particularly evident during the suppressed phase following deep convection (day +5 to +20), at the day-0 maximum q' (40% larger in SP-CAM) and in the persistent positive q' below 800 hPa throughout the model's MJO life cycle. As will be discussed in section 5, an unrealistic feedback between convection, surface fluxes, and SSTs in the simulation setup might contribute to this positive moisture bias.

The fundamental elements of the evolving MJO temperature structure (Figs. 4c,g) are captured by the SP-CAM. In both composites, low-level warm anomalies lead heavy precipitation by one to two weeks. When rainfall is most intense near day 0, upper-level T' is maximized as significant negative anomalies develop near the tropopause and below the tropical freezing level (550 hPa). Radiosonde-based studies (Lin and Johnson 1996; Kemball-Cook and Weare 2001; KSH05) that diagnose the evolving vertical temperature structure during an MJO passage have shown that maximum

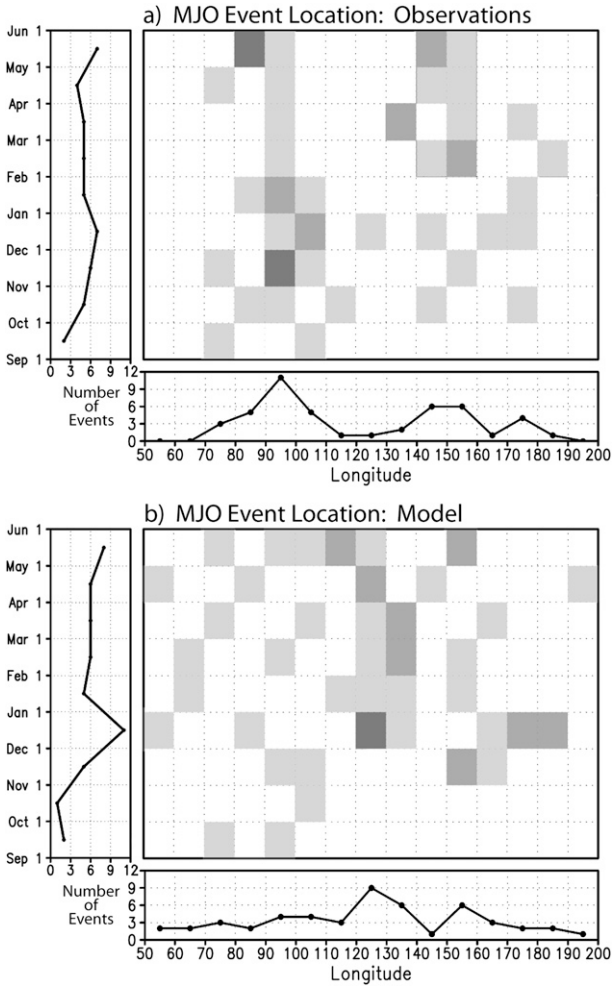

FIG. 3. Time and longitude information of all identified MJO events from (a) GPCP and (b) SP-CAM rainfall. Shaded squares in the grid represent the time and longitude (binned by month and 10° span) of maximum rainfall intensity associated with each MJO event. Lightest (darkest) shading represents 1 (3) event(s) occurring during that particular month and longitudinal bin. Horizontal and vertical line plots display cumulative event numbers based on longitude and month, respectively.

upper-tropospheric warmth typically occurs within five days of the deepest convection, in concert with the simulated composite results here. Together, the composite plots of T' (Figs. 4c,g) and q' (Figs. 4b,f) depict well-documented features of the MJO: low-level warming and moistening on days -15 to -10, suggesting shallow convection development; deep-layer positive T' and q' on days -10 to -5, reflecting deep convective processes; and ''top-heavy'' profiles of T' and q' on days -5 to $+5$, indicating a transition to stratiform precipitation processes (e.g., KSH05).

Despite capturing many features of the observed MJO temperature structure, several model deficiencies exist. The SP-CAM has insufficient cooling in the middle to upper troposphere during the MJO suppressed phase (Fig. 4g). The model tends to redevelop significant low-level warm anomalies during the postconvective suppressed phase (days +7 to +16), where no such warming is seen in observations. Additionally, the magnitude of simulated 300-hPa T' maximum on day 0 is nearly 50% larger than in nature. Important boundary layer features differ between the model and reanalysis as well. In the SP-CAM, low-level warmth prior to deep convection develops first within the boundary layer beginning near day -20, whereas in ERA-40 initial warmth is seen first at 700 hPa and significant boundary layer warming is delayed until about day -12. Also, the SP-CAM produces a well-developed boundary layer cold pool (near-surface $T' = -0.6$ K on day 0; Fig. 4g), likely the result of vigorous convection and abundant boundary layer rain evaporation. Owing to its coarser vertical resolution and strong dependence on parameterizations over the open ocean, the reanalysis could have difficulty accurately capturing the low-level stratiform precipitation signature and evaporative cooling within the boundary layer. Radiosonde-based results show that day-0 meridionally averaged boundary layer cooling does not exceed -0.4 K for the composite MJO (KSH05), further suggesting an overestimation by the SP-CAM. Fluctuations of boundary layer moisture and temperature are an essential aspect of intraseasonal convective episodes (Wang 1988; Maloney and Hartmann 1998; Kemball-Cook and Weare 2001), and capturing such variability in GCMs is likely a critical step toward simulating a realistic MJO.

The composite time series of total rainfall for SP-CAM, GPCP, and their difference are shown in Fig. 4d (and repeated in Fig. 4h). For the composite of all MJO events, the SP-CAM consistently overestimates rainfall during all phases of the MJO by 1–2 mm day^{-1}. As we will see shortly, these biases are mainly associated with MJO disturbances whose peak rainfall rates occur in the west Pacific rather than the Indian Ocean or Maritime Continent sectors. The greatest departures from observations occur during the 10 days leading up to deepest convection and at two weeks following heaviest rainfall as the suppressed phase emerges. When rainfall is most intense (day 0, Fig. 4d), the SP-CAM out-precipitates GPCP by 20%. These overestimations of precipitation combined with the excessive warmth, moisture, and zonal circulation reflect the model's tendency to produce MJO convection that is too vigorous, particularly for west Pacific disturbances.

Cross sections of equivalent potential temperature θ_e', which behaves similarly to moist static energy, are displayed in Figs. 5a,b for ERA-40 and SP-CAM,

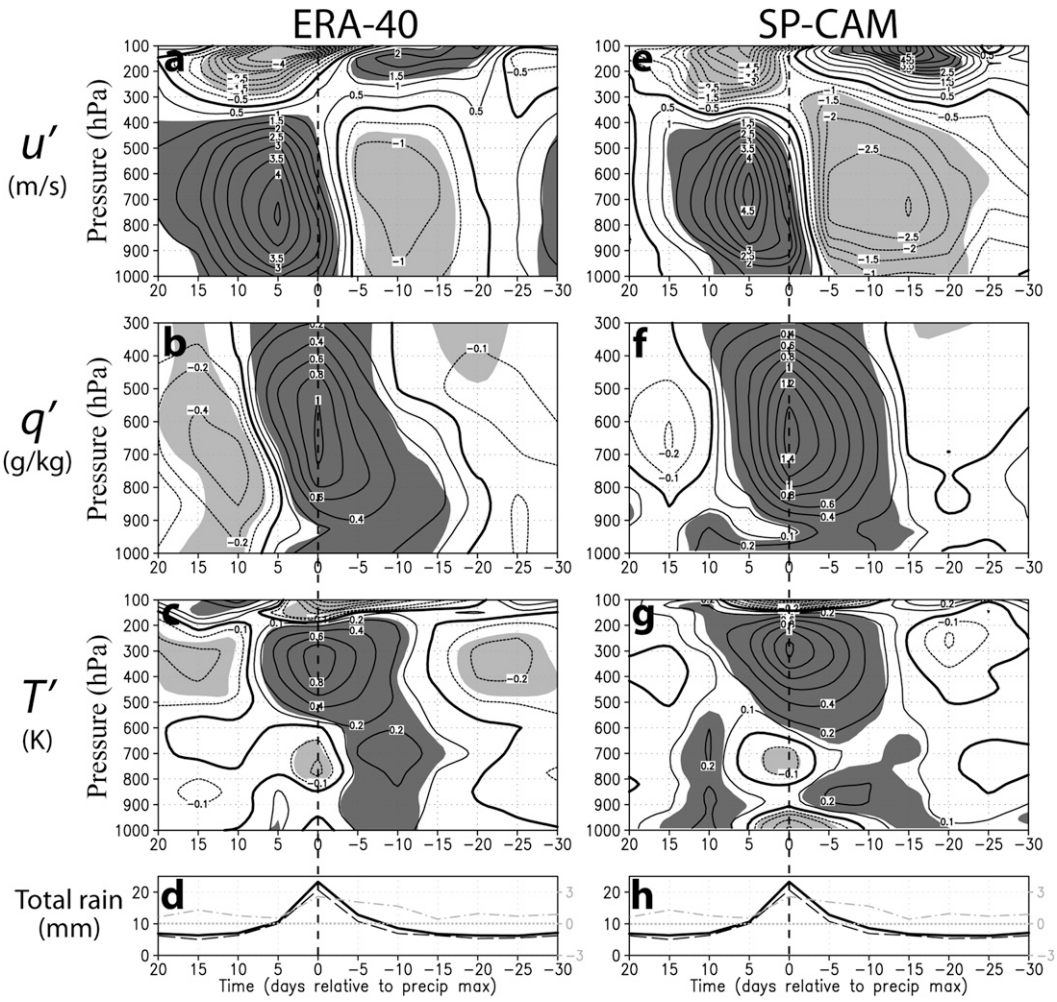

FIG. 4. Composite time–height plots of (top) anomalous zonal wind u', (middle) specific humidity q', and (bottom) air temperature T' based on (left) ERA-40 data and (right) SP-CAM output. Composites contain all identified MJO events within their respective data sources. Thin solid, thin dashed, and thick solid lines display the positive, negative, and zero contours, respectively; dark (light) shading indicates areas of statistical significance greater than 95% for positive (negative) anomalies. In the bottom row, composite time series of rainfall from GPCP (dashed black), SP-CAM (thick solid black), and their difference (SP-CAM − GPCP; dotted–dashed gray) are shown.

respectively. Positive departures of θ_e' develop first in the lower troposphere below about 800 hPa in both composites. Deepening convective clouds rooted in the boundary layer loft high-θ_e air into the free troposphere between days −15 and −10 as θ_e' becomes negative near 100 hPa. The lofting of high-θ_e air near day −10 is too rapid in the SP-CAM (Fig. 5b) compared to reanalysis (Fig. 5a), suggesting a premature yet intense onset of MJO-related deep convection in the model that is confirmed by the rainfall bias in Fig. 5c. We see that θ_e' is also uniformly too positive in the SP-CAM, particularly below 800 hPa during the suppressed phase. This observation is consistent with the SP-CAM's positive bias regarding low-level T' and q' during the suppressed phase (Fig. 4). Additionally, simulated maximum perturbations of θ_e' on day 0 are slightly lower in altitude and greater in magnitude than those in nature.

Composite time series of simulated and observed precipitable water anomalies (Fig. 6a) indicate a gradual moistening during the two weeks preceding deep convection followed by a more rapid decline in moisture to below-climatological values after the heaviest rainfall. Except for day −15, simulated PW is consistently 0.5–2.0 mm wetter than observations. This wet bias, which matches the q' plots of Fig. 4, along with the SP-CAM's persistent overestimation of precipitation (dashed line in the bottom panel of Fig. 6), is most notable one to two pentads prior to heaviest rainfall as well as during the drying phase of the MJO (days +5 to +15). Despite these discrepancies, the time evolution of

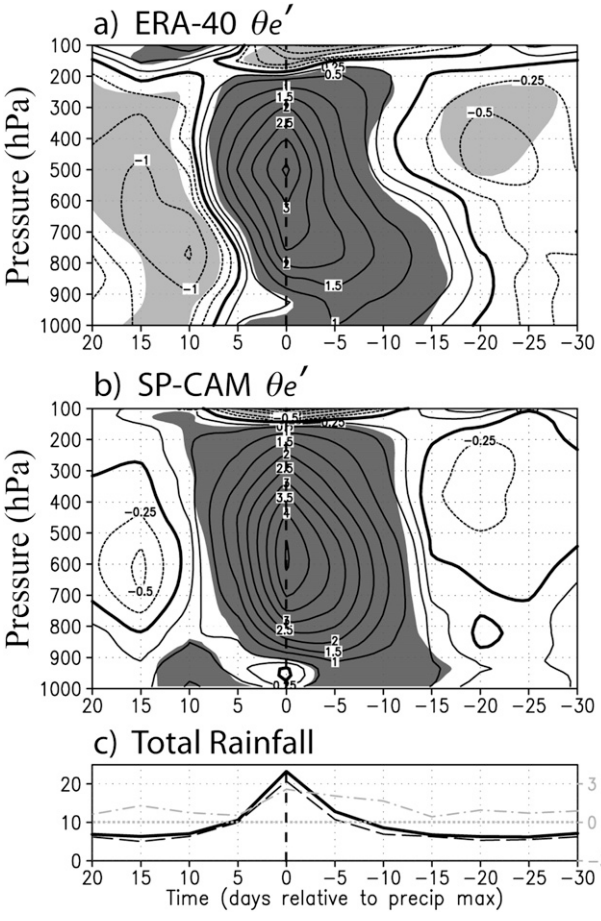

FIG. 5. As in Fig. 4, but for equivalent potential temperature θ_a' for (a) ERA-40 and (b) SP-CAM.

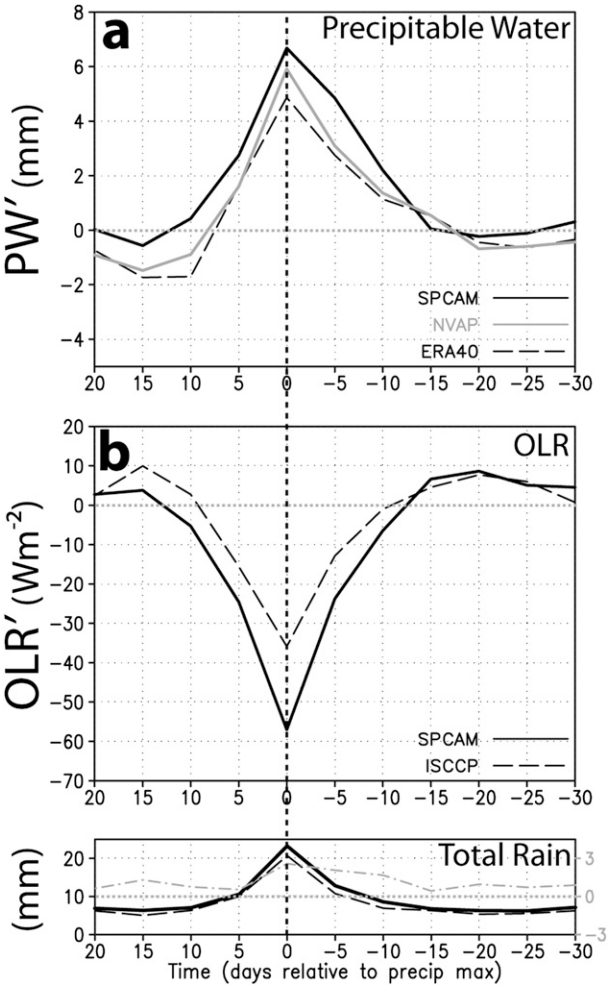

FIG. 6. Time series of (a) PW′ and (b) OLR′ during the MJO life cycle. Data sources for PW′ include SP-CAM (solid black), NVAP (solid gray), and ERA-40 (dashed black); OLR′ sources include SP-CAM (solid black) and ISCCP (dashed black). Composites contain all identified MJO events within their respective data sources. Rainfall plot at bottom is identical to Fig. 5c.

simulated PW′ closely follows observations and the magnitude of the maximum anomaly is only 10% larger than NVAP satellite-based measurements.

Simulated and remotely sensed OLR perturbations are displayed in Fig. 6b and support the theme of unrealistically intense convection in the SP-CAM during the peak of the MJO wet phase. Composite OLR′ based on all simulated MJO events is more negative than ISCCP-based composites, especially within two weeks before and after maximum MJO-related rainfall.

d. Structure of derived quantities

Convective heating and advective moisture transport are two complex yet fundamental processes associated with the MJO. Because such processes involve several dynamic and thermodynamic variables, their accurate representation is a critical test of the SP-CAM's ability to produce realistic MJO disturbances.

We examine the anomalous apparent convective heating Q_1', representing both cumulus and stratiform heating and radiative effects, in pressure–longitude space rather than pressure–time space as in Figs. 4–6. Having longitude rather than time along the horizontal axis better illustrates the westward tilt of Q_1' with height (see Lin et al. 2004), a feature that was less clear using the coarser pentad time resolution from previous plots. For Fig. 7, we again utilize MJO filtered signals as a guide to construct composites of the unfiltered field. For a given MJO disturbance (previously identified in section 3), we scan the times during which its MJO convective envelope overlaps a chosen longitude (for Fig. 7 this is 160°E). We select the pentad corresponding to the maximum in unfiltered meridionally averaged rainfall at that chosen longitude and call this the *base time.* We then composite the unfiltered meridionally averaged Q_1'

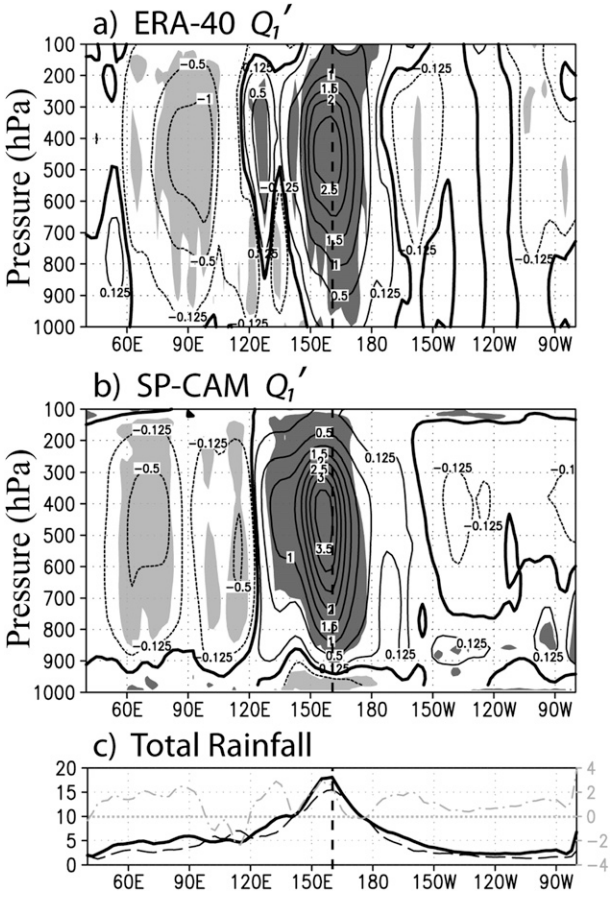

FIG. 7. (a),(b) Longitudinal cross section of anomalous apparent convective heat source Q_1', averaged between 10°S and 5°N, at a fixed time corresponding to maximum MJO-related rainfall at 160°E for (a) ERA-40 and (b) SP-CAM. Contours and significance shading are identical to Fig. 4. (c) Corresponding longitudinal profile of rainfall displays observed, simulated, and difference rainfall values as in Fig. 4.

field in pressure–longitude space referenced to this base time. Figure 7 displays longitudinal cross sections of Q_1' and total rainfall averaged between 10°S and 5°N. Both heating profiles (Figs. 7a,b) are qualitatively similar, with midlevel maxima near 450 hPa within 4°–8° longitude (1–2 days, assuming a 5 m s^{-1} MJO phase speed) of heaviest rainfall, lingering heating above 500 hPa to the west of the deep heating, and deep-layer negative anomalies west of 120°E reflecting suppressed-phase radiative cooling. The model, however, tends to produce a maximum heating value that is larger than observed, does not produce as clear a mesoscale stratiform signal in the MJO wake (120°–140°E), and has weaker and westward-shifted suppressed-phase radiative cooling (negative Q_1') over the Indian Ocean. The SP-CAM fails to produce weak but significant negative Q_1' values in the middle troposphere prior to the heaviest rainfall (near 160°W) and in the lower troposphere during the time when stratiform processes are active (near 130°E). At both of these longitudes, simulated rainfall is notably higher than observed rainfall. We can therefore infer that deep convective processes are not as weak as they should be at these locations relative to maximum MJO rainfall.

Returning to the pressure–time composite framework, we next examine horizontal divergence. Observed boundary layer convergence (Fig. 8c) develops approximately two weeks prior to heavy rainfall and is followed by stronger, deep-layer convergence on day 0, lingering weaker convergence at midlevels through day +10, and finally upper-level convergence after day +10. A very similar vertically tilted structure is noted in the simulated divergence field (Fig. 8f), although maximum convergence (divergence) magnitudes at lower (upper) levels on day 0 are substantially larger than those in Fig. 8c. Additionally, the SP-CAM composite of 50 events does not show a consistent low-level divergence pattern after day +10 when compared to statistically significant divergence values in ERA-40.

In nature and in the model, boundary layer convergence prior to deep convection is primarily associated with the meridional component (Figs. 8b and 8e, respectively). This shallow convergence layer develops as early as day −20 and counteracts weak zonal divergence as seen in the reanalysis composite (Fig. 8a). Boundary layer convergence extending well ahead of mature MJO convective disturbances is described by the ''frictional convergence feedback.'' This mechanism has been well documented in numerous studies and is thought to play an important role in preparing the atmosphere for deep convection via destabilization (Wang 1988; Salby et al. 1994; Maloney and Hartmann 1998).

Displayed in the top row of Fig. 8, deep-layer zonal convergence from the surface to 350 hPa is accomplished by a rapid deceleration of easterly (westerly) zonal winds preceding (following) MJO-related deep convection near day 0 (see Fig. 4). Lingering zonal convergence above 500 hPa between days +5 and +10 reflects the transition from convective to stratiform cloud processes, with midlevel convergence sandwiched between divergent (or less convergent) layers above and below. Insufficient (or inconsistent, from event to event) simulated zonal divergence, noted in Fig. 8d between the surface and 500 hPa after day +10, can be traced back to the premature weakening of low-level westerly anomalies in the SP-CAM relative to reanalysis (Figs. 4e and 4a, respectively). Additionally, weaker low-level zonal divergence in the model prior to deep convection (Fig. 8a) is linked to suppressed-phase easterlies that are too extensive and fairly uniform in magnitude (cf. Figs. 4e and 4a).

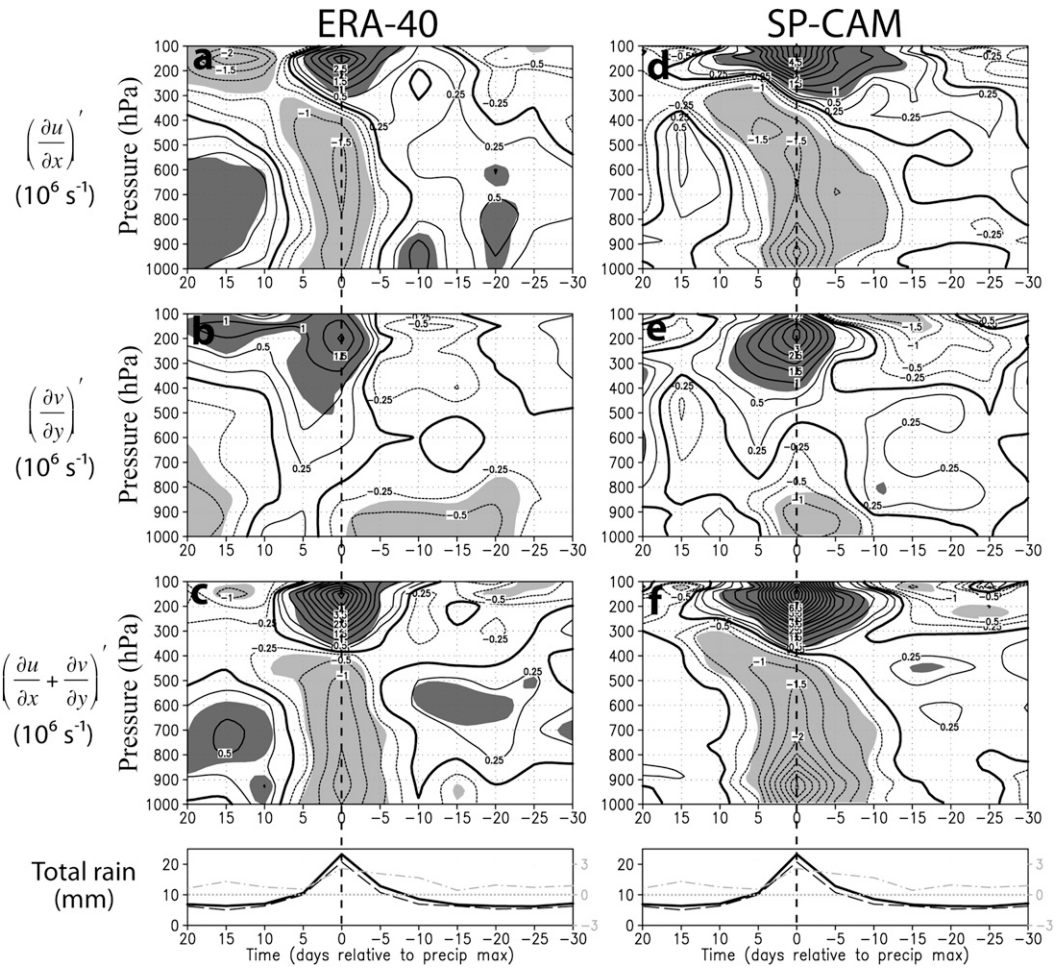

FIG. 8. As in Fig. 4, but for zonal divergence, meridional divergence, and total horizontal divergence.

Figure 9 presents the total horizontal components of the advective form of the moisture budget equation.[1] As demonstrated by Arakawa (2004), components of the moisture budget equation in advective form more directly and accurately represent temporal changes in q. The plots of total horizontal moisture advection indicate that deep-layer moistening occurs prior to the onset of the MJO wet phase. At this time (days -20 to -10), advective moistening within the boundary layer is achieved by the zonal component while meridional moisture convergence is noted in the free troposphere (not shown). Vertical moisture transport (not shown) dominates between days -10 and $+5$ and, because Q_1' is positive and nonnegligible at this time, this moistening by large-scale vertical advection is likely a manifestation of widespread deep convection and its associated detrainment on subgrid scales. In both the model and observations, large-scale horizontal advective drying commences just before heaviest precipitation and is maximized between days 0 and +5 at 650 hPa (Fig. 9). Although the moisture budget on day 0 is dominated by moistening from the vertical component, the rapid decrease in q' between days 0 and +5 can be mostly attributed to horizontal advective drying because $[-\omega(\partial q/\partial p)]'$ remains positive through day +5 (not shown). Lower tropospheric drying linked to horizontal advection following the MJO has been discussed in previous studies (e.g., Maloney and Hartmann 1998; Benedict and Randall 2007). Overall, the SP-CAM composites compare very favorably with those of ERA-40, accurately capturing key advective features throughout the MJO life cycle.

e. Longitudinal dependence of MJO structure

Our compositing technique pinpoints the time and longitude of maximum unfiltered rainfall during an MJO

[1] Condensation (C) and evaporation (E) are not analyzed because of measurement difficulty. On the time and space scales considered, C and E are assumed small compared to the advective components.

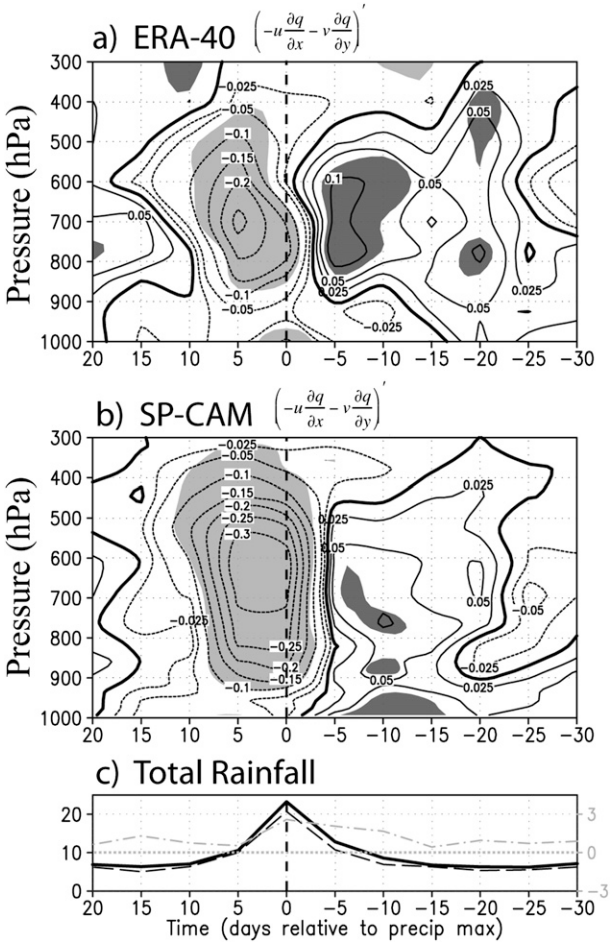

FIG. 9. As in Fig. 5, but for horizontal moisture transport.

disturbance. Owing to this procedure, we can subset the list of all MJO events by categorizing them based on their tagged longitudes. This subsetting allows us to examine the differences in dynamic and thermodynamic structure of the MJO as a function of the longitude at which each event reaches its peak intensity.

Table 2 gives the number of MJO events for each longitudinal sector. Time–height composites of u' for each sector are displayed in Fig. 10. The SP-CAM captures the longitudinal-dependent timing and vertical structure of westerly anomalies remarkably well. In the Indian Ocean sector, anomalous low-level easterlies transition to westerlies only one to two days prior to maximum rainfall in the reanalysis composite (Fig. 10a). This transition is uniform with height from the surface to 500 hPa, and the maximum westerlies occur about one pentad following peak rainfall (Fig. 10c). A similar transition is noted in the SP-CAM Indian Ocean composite (Fig. 10b), although somewhat greater inconsistency among events in the westerly onset is reflected by the lower significance

TABLE 2. The number of MJO events recorded in each longitudinal sector. The event location is defined as the longitude at which the MJO disturbances maximum rainfall occurred. ''Observations'' here refers to the ERA-40 dataset.

	Observations	Model
Indian Ocean MJO events (50°–100°E)	15	13
Maritime Continent MJO events (100°–145°E)	14	22
West Pacific MJO events (145°E–170°W)	17	15
Total	46	50

values. Simulated and observed MJO disturbances in the Maritime Continent sector both indicate a slightly earlier onset of low-level westerlies (3–4 days before peak rainfall) and a more pronounced vertical tilting (Figs. 10d and 10e, respectively). MJO events in the west Pacific tend to have an even earlier onset of westerlies relative to maximum rainfall. In both model and reanalysis (Figs. 10h and 10g, respectively), westerly onset within a deep layer from the surface to 400 hPa occurs 5–6 days before intense rainfall for west Pacific events. Although there are noted differences between the wind structures of the SP-CAM and ERA-40 (e.g., the magnitudes of low-level Indian Ocean westerlies), the general character of the easterly-to-westerly transition in the model compares favorably with nature.

Figure 11 displays more clearly the consistent behavior of low-level (925 hPa) westerly wind onset between the SP-CAM and reanalysis composites. For events with peak convective intensities in the Indian Ocean sector, both the model and reanalysis (thick solid gray and thick dashed gray lines in Fig. 11, respectively) indicate that total (not shown) and anomalous low-level winds are decidedly easterly on day −5 and weakly westerly on day 0. For MJO events farther east in the Maritime Continent sector, we can infer that this transition is slightly earlier in nature and the SP-CAM (dashed and solid dark gray lines in Fig. 11, respectively). The earliest onset of low-level westerly wind anomalies is noted for west Pacific events, with the strongest westerlies nearly coincident with maximum rainfall for the reanalysis and simulation composites (thin dashed black and thin solid black lines, respectively). This shift in maximum surface westerlies—from several days after heaviest precipitation to being coincident with it—has been extensively documented using in situ measurements (Zhang and McPhaden 2000).

f. Composite maps

Figures 12 and 13 present the spatial structure of MJO disturbances with maximum rainfall centers in the eastern

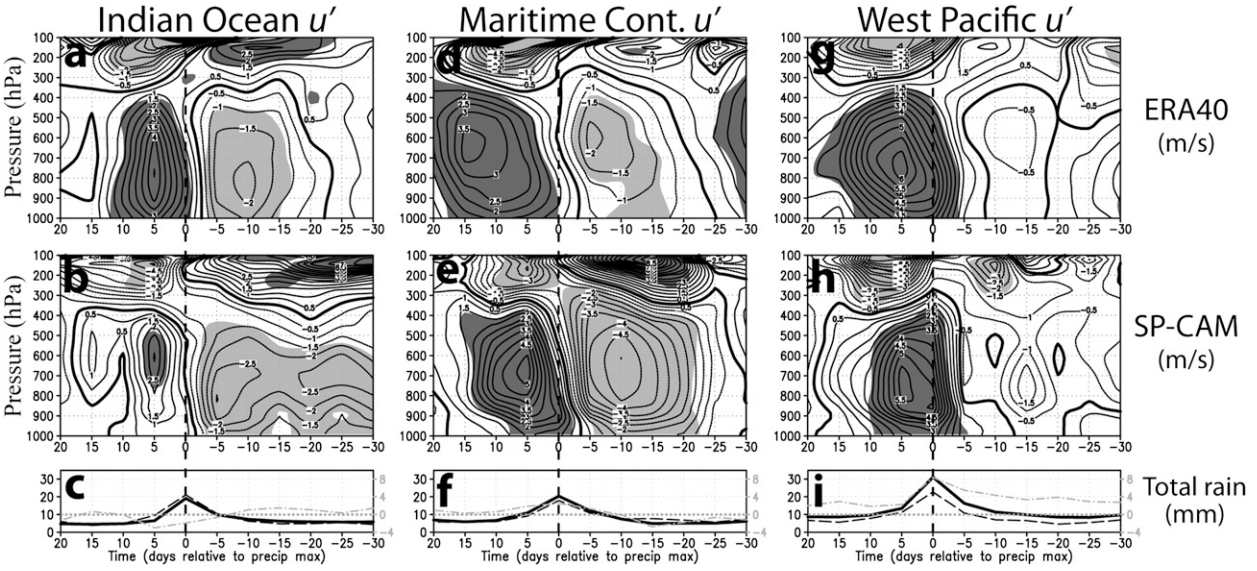

FIG. 10. A comparison between (top) ERA-40 and (middle) SP-CAM composite anomalous zonal wind u' for the (left) Indian (50°–100°E), (middle) Maritime Continent (100°–145°E), and (right) west Pacific sectors (145°E–170°W). Composites are based on any identified MJO events that have their maximum intensity in the indicated longitudinal sector. Thin solid, thin dashed, and thick solid lines display the positive, negative, and zero contours, respectively; dark (light) shading indicates areas of statistical significance greater than 90% for positive (negative) anomalies. (bottom) Composite time series of rainfall corresponding to the indicated longitudinal sector are shown, including GPCP (dashed black), SP-CAM (thick solid black), and their difference (SP-CAM − GPCP; dotted–dashed gray).

Indian and west Pacific sectors, respectively. We follow a similar procedure used to produce Fig. 7 (see section 4d) but now construct composites in longitude–latitude rather than pressure–longitude space. Overall, the simulated spatial composites exhibit consistency with observations. Owing to the chosen seasonal range, precipitation centers occur as a single maximum just south of the equator and are flanked by negative rainfall anomalies to the east and west (shading in Figs. 12a,b and 13a,b). The spatial scale of the rainfall anomalies in the SP-CAM compares well with that in the GPCP-based composite. The 850-hPa anomalous horizontal wind fields are similar, with westerly anomalies mainly lagging the 90°E rainfall center but leading the 160°E rainfall center (vectors in Figs. 12a,b and 13a,b). Easterly anomalies to the east of the disturbance are stronger when the rainfall center is in the Indian Ocean. In both the model and observations, maximum positive precipitable water anomalies occur just ahead of the rain centers and are of comparable magnitude (Figs. 12c,d and 13c,d). Additional analyses (not shown) reveal that other well-documented features of the MJO are seen in the SP-CAM spatial composites: 1) low-level positive moisture anomalies, convergence, and rising motion occur well ahead of the disturbance where rainfall anomalies are still negative; 2) low-level divergence and subsidence are noted in the wake of the disturbance (Maloney and Hartmann 1998); and 3) anomalous surface latent heat fluxes are negative (positive) before (after) the rain center (Jones and Weare 1996).

Several differences between the spatial composites of the simulation and observations must be addressed. Possibly arising from the greater magnitude of equatorward flow from the drier subtropics (Figs. 12a,b and 13a,b), bands of more substantial negative rain anomalies straddle the equator ahead of the rain centers in the SP-CAM, particularly for the Indian Ocean composite. Greater meridional flow in the model is also noted at upper levels (not shown), and Rossby gyres are stronger and shifted equatorward compared to observations. Consistent with the rainfall time series of Fig. 10, simulated peak rain anomalies are weaker (stronger) for the Indian Ocean (west Pacific) composites. Additionally, the redevelopment of easterly anomalies in the west Indian Ocean is delayed in the model (cf. Figs. 13a,b), possibly suggesting a slower re-emergence of the next MJO event. Perhaps the most notable discrepancy, as previously discussed in section 4c, is the significantly weaker atmospheric drying in the wake of simulated MJO disturbances. In the Indian Ocean, trailing rainfall anomalies to the southwest of the rain center are more positive in the model and trailing negative moisture anomalies are shifted northward off the equator (Figs. 12c,d). Insufficient atmospheric drying in the model is clearer for west Pacific events (Figs. 13c,d). In this region, simulated negative anomalies of rainfall and

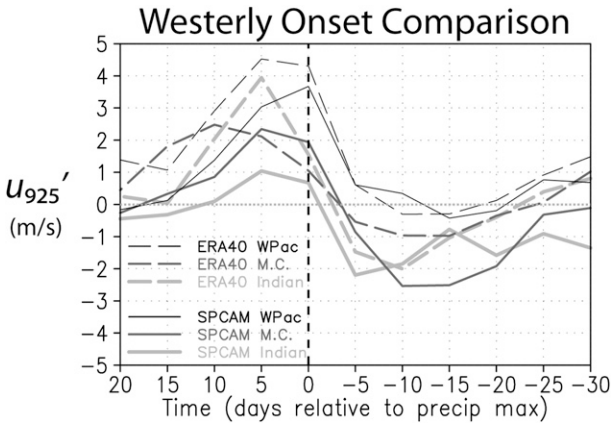

FIG. 11. A comparison between ERA-40 (dashed) and SP-CAM (solid) of anomalous zonal winds at 925 hPa for the longitudinal sectors examined in Fig. 10.

moisture in the MJO wake are weaker and shifted westward by 30° to the west Indian Ocean. The absence of strong drying following heavy rains in the SP-CAM could be partially tied to the model's prescribed SSTs. In Figs. 12e,f and 13e,f, warm SSTs[2] lead heavy rains, but the substantial cooling seen in nature following the precipitation maximum is nonexistent in the model. Consistent with this lack of ocean surface cooling, negative anomalies of low-level q and θ_e are weaker and surface flux anomalies are higher in the model (not shown). A more detailed discussion of the atmosphere–ocean feedbacks in relation to the simulated MJO is presented next.

5. Discussion and conclusions

a. The west Pacific MJO intensity bias

We have demonstrated that the convective intensity of the all-event composite MJO is greater in the SP-CAM than in observations. A closer examination indicates that such biases are relatively small for events in the Indian Ocean and much larger for west Pacific (WP) events. For example, root-mean-square errors of total precipitation over the composite MJO life cycle are 1.4, 1.5, and 4.1 mm day^{-1} for events in the Indian, Maritime Continent, and WP sectors, respectively (e.g., bottom panels of Fig. 10). Additional metrics based on other atmospheric variables (not shown) also reveal the overestimated intensity of WP MJO events. Although a more detailed and definitive explanation is beyond the scope of this paper, we will mention several factors that may contribute toward the positive intensity bias of simulated WP MJO disturbances.

Possible origins of the intense WP MJO events may be linked to the lower boundary conditions when such disturbances are active. Figure 14 displays the behavior of several boundary layer variables during the MJO life cycle for events in the Indian and WP sectors. Composite time series of SST′ (Figs. 14a,b) indicate that simulated MJO disturbances tend to have their maximum rainfall rates in the WP when SSTs there are warmer than climatology, whereas SST′ values for events farther west are more similar to observations. The preference of the model to produce WP MJO events when prescribed SST values in that region are warm—in combination with other factors [e.g., substantially stronger surface fluxes (cf. Figs. 14c,d) and a more developed moisture convergence signal (not shown)]—would contribute to an increased likelihood and intensity of simulated deep convection (Maloney and Hartmann 1998). These processes linking anomalously warm SSTs, overestimated air–sea energy exchange, and enhanced moisture convergence may help to explain the model's tendency to favor the development of organized convection of greater intensity, and this seems particularly true in the WP region. We also note that three (of 15 total) events in the SP-CAM WP composite occurred after the end of the selected observational data range and at a time when SSTs were above their long-term average.

In nature, tropical convective intensity is regulated by downdrafts that inject cooler and drier air into the boundary layer, generally resulting in increased surface winds, enhanced surface fluxes, and cooler SSTs (Zipser 1969; Houze 1982; Lin and Johnson 1996; Zheng et al. 2004; see also dashed lines in our Figs. 14f,d,b, respectively). Although downdrafts and robust convectively generated cold pools exist in the SP-CAM (e.g., Fig. 4g), the feedback connection is incomplete because the prescribed SSTs are unaffected by the surface energy fluxes (solid lines in Figs. 14a,b). In the model, the combination of enhanced, convectively driven surface fluxes and unmodulated SSTs could maintain or more rapidly restore boundary layer θ_e and lead to an increased probability of future convection (e.g., Raymond 1995). Additional factors such as the ''recycling'' of small-scale convective systems across the periodic CRM boundary may also contribute to this problem, termed the ''convection–wind–evaporation feedback.'' Adaptations of this theory, originally proposed by Emanuel (1987) and Neelin et al. (1987), have been shown to play an important role in organized tropical convection on many scales, as seen in observations (e.g., Hendon and Glick 1997),

[2] Although SST in the model is prescribed using observations from 1985 to 2004, we can treat these data as we would any other variable and form composites based on simulated maximum rainfall.

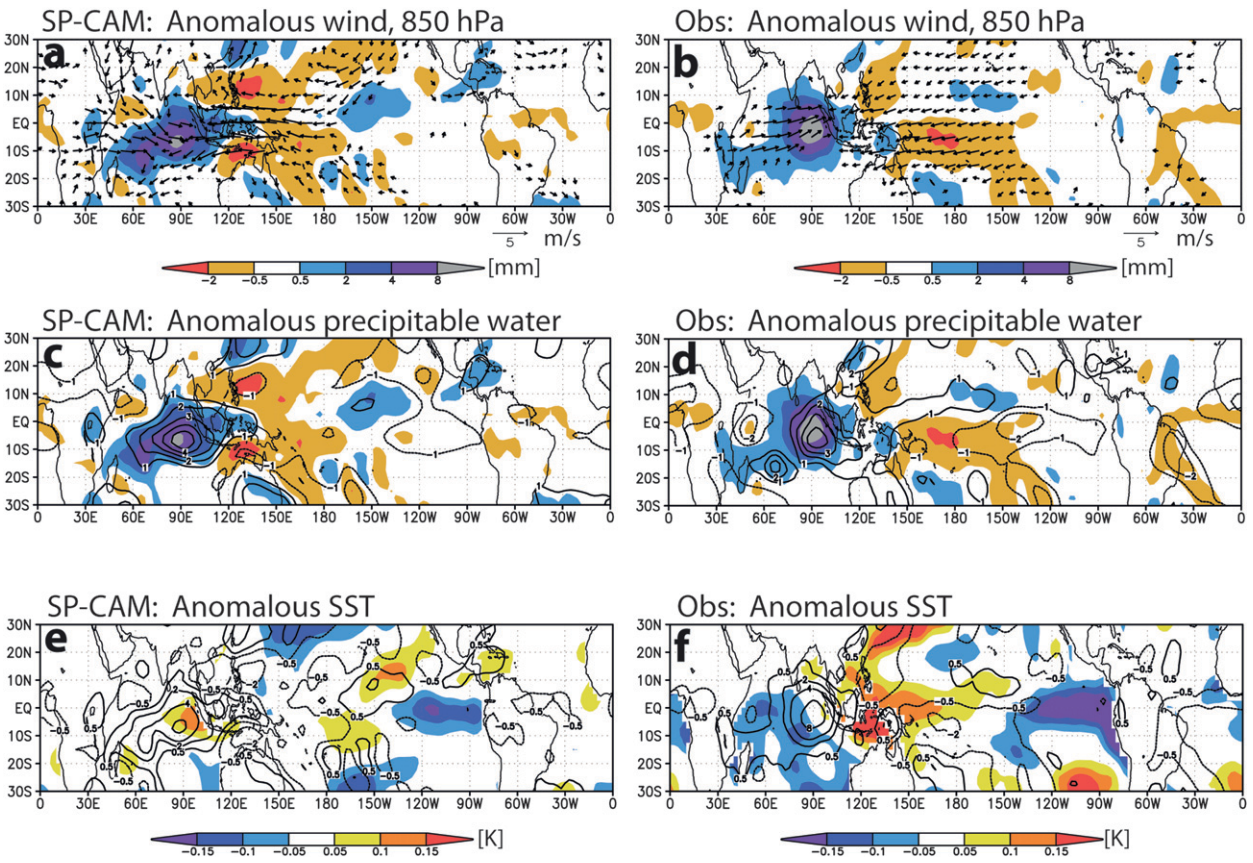

FIG. 12. Composite plots of (top) anomalous 850-hPa wind, (middle) PW, and (bottom) SST for (left) simulated and (right) observed MJO events with rainfall maxima at 90°E. Rainfall anomalies are shaded in the top two rows and contoured in the bottom row. Anomalies are based on departures from the long-term boreal winter mean. Shading and contours correspond to significance levels above 90% in the tropics. Approximately 40 MJO disturbances contribute to each composite.

conventional GCM simulations (Zhang 1996; Maloney and Sobel 2004), GCM simulations using superparameterization (Luo and Stephens 2006), or CRM simulations (Wang et al. 1996).

To further investigate the potential role that convection–wind–evaporation feedback may play regarding WP MJO biases in the SP-CAM, we examine the components of surface latent heat flux during the MJO life cycle (Fig. 14). We have established that simulated MJO disturbances in the WP have higher SST′ (Figs. 14a,b) and consistently heavier rains (Figs. 14k,l) compared to Indian Ocean events. In this region, near-surface (992 hPa) q is considerably higher in the model compared to observations (not shown) and contributes to a sharper vertical gradient of q within the boundary layer (Fig. 14h). This, combined with generally stronger boundary layer winds (Fig. 14f; see also Thayer-Calder and Randall 2009), is linked to substantially larger simulated surface heat fluxes (25%–30% greater than ERA-40; Fig. 14d) throughout the lifetime of the simulated WP MJO disturbance. The ERA-40 total surface flux composite values in the active and suppressed MJO phases closely match composite in situ measurements presented in Zhang (2005), signaling that the SP-CAM is indeed overestimating surface fluxes during MJO disturbances. A distinguishing feature of simulated WP MJO events involves boundary layer θ_e. Large vertical gradients of θ_e within the boundary layer are seen in the SP-CAM (not shown), particularly during the heaviest rains, and are the result of warmer near-surface θ_e (relative to reanalysis) and cooler θ_e near the upper boundary layer. As in any observed MJO event, θ_e at 992 and 925 hPa for simulated Indian Ocean events decreases as heavy MJO rains develop near day −5 (e.g., Fig. 14i), implying the emergence of mechanisms that act to dissipate deep convection as discussed previously. In stark contrast, the reduction of boundary layer θ_e during heavy rains is nonexistent for simulated WP MJO events (Fig. 14j), with θ_e at 992 hPa steadily *increasing* between days −15 and +10 (not shown). Simulated Indian Ocean MJO events generally have less rainfall (Fig. 14k) and weaker near-surface winds (Fig. 14e), boundary layer

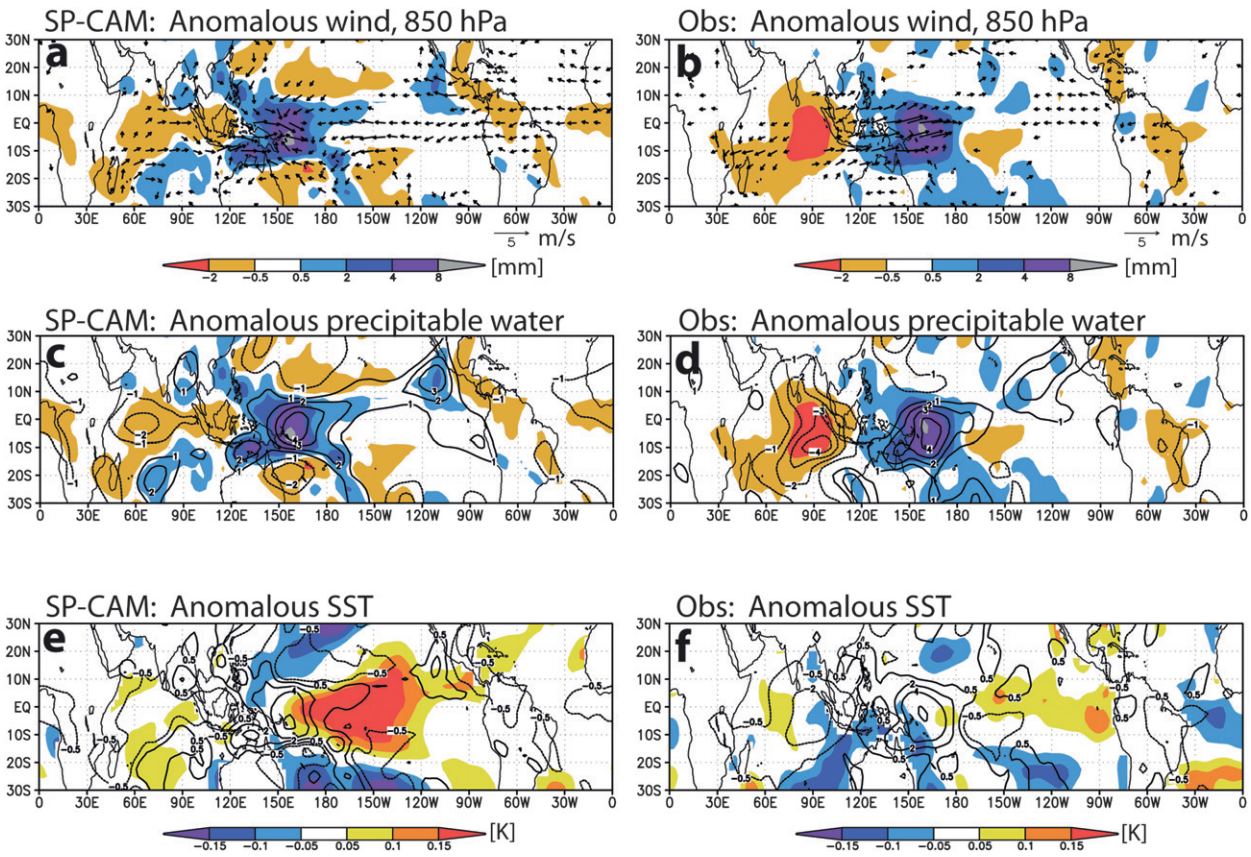

FIG. 13. As in Fig. 12, but for MJO events with rainfall maxima at 160°E.

moisture gradients (Fig. 14g), and surface fluxes (Fig. 14c) compared to WP events. Although additional factors are undoubtedly involved, the convection–wind–evaporation feedback and its interaction with elevated SST′ appear to play an important role with regard to the WP MJO bias in the SP-CAM.

Differences in topography and the mean state may also contribute to the biases of simulated WP MJO events. In nature, MJO events tend to weaken and become disorganized over the Maritime Continent region in association with altered air–sea interactions and a disruption of the low-level wind field (e.g., Maloney and Hartmann 1998; Inness and Slingo 2006). Our results support these findings and indicate reductions in peak rainfall amounts and maximum convective heating rates for observed MJO events over the Maritime Continent (see Fig. 10 for rainfall comparison; heating rates not shown). We find, however, that MJO events in the SP-CAM do not weaken as they cross the Maritime Continent. Simulated and observed MJO events over the Indian Ocean have similar maximum convective heating rates and show a tendency of increased heating as the disturbances propagates eastward. Observed MJO events then weaken as they encounter Indonesia, whereas MJO intensity is maintained or slightly elevated in the SP-CAM. The sustained heating for simulated Maritime Continent MJO events generates a more vigorous dynamic response (Figs. 10d,e) and is associated with an environment more favorable for MJO intensification over the WP region. For example, comparing observed and simulated MJO disturbances with rainfall centers over the Maritime Continent (120°E), lower tropospheric convergence over the WP is 2 to 3 times stronger in the SP-CAM (not shown). The lack of MJO weakening over the Maritime Continent and sustained low-level convergence ahead of the disturbance may be yet another factor related to the WP MJO bias. Differences between simulated and observed boreal winter mean states must also be considered. In the equatorial WP region, climatological surface latent heat fluxes are 20–35 W m^{-2} (20%) higher in the SP-CAM compared to nature, but surface flux differences of only ±5 W m^{-2} are noted in the equatorial Indian Ocean. Simulated boreal winter mean vertical wind shear is also significantly weaker in the Indian Ocean region compared to observations, whereas slightly positive WP vertical shear biases exist in the model. While it is unclear exactly what impact these differences in the mean state could have on the MJO, we

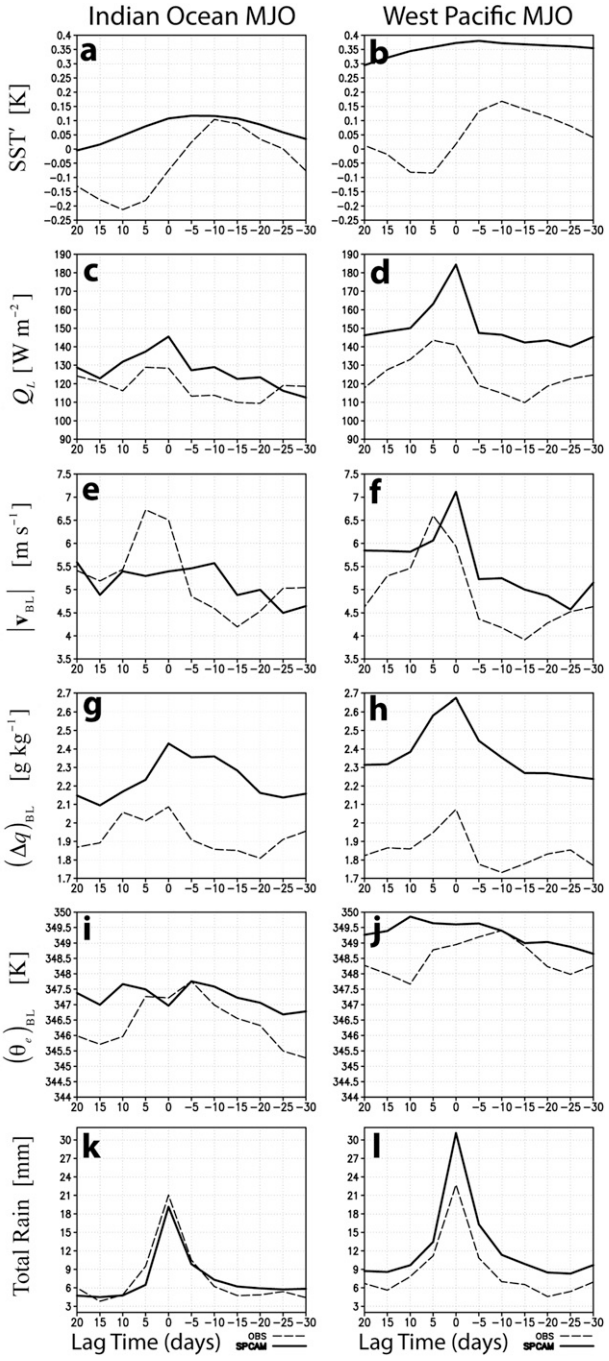

FIG. 14. Composite time series of boundary layer fields during the life cycle of MJO disturbances in the (left) Indian Ocean and (right) west Pacific. Displayed from top to bottom are SST anomaly, total surface latent heat flux Q_L, boundary layer-averaged ["BL"; (992 hPa + 925 hPa)/2] wind magnitude $|\mathbf{v}_{BL}|$, BL difference (992–925 hPa) of specific humidity $(\Delta q)_{BL}$, BL total equivalent potential temperature $(\theta_e)_{BL}$, and total rainfall for observations (dashed) and SP-CAM (solid). Domain boundaries are listed in the Fig. 10 caption. ERA-40 data are used as observed fields for all but SST′ (OISST2) and rainfall (GPCP).

have demonstrated that many complex factors likely contribute to the WP MJO intensity bias in SP-CAM.

b. Summary

In this study we conduct a detailed comparison of the space–time structure of MJO disturbances between the superparameterized Community Atmosphere Model version 3.0 (SP-CAM) and observational datasets. Tropical intraseasonal variability is unrealistically weak in many GCMs (Lin et al. 2006), but the newly developed approach of embedding a collection of cloud-resolving models into each GCM grid cell to explicitly simulate subgrid-scale cloud processes gives a realistic depiction of the MJO (KDR08). Whereas previous studies have only done a cursory analysis of intraseasonal variability in the SP-CAM using spectral characteristics and simple measures of variance (e.g., Khairoutdinov et al. 2005; KDR08), our work examines in much greater detail the composite MJO structure and the fundamental convective, advective, and boundary layer processes that affect it.

Our analysis demonstrates that the AMIP-style simulation examined here compares favorably with observation-based datasets regarding many aspects of the composite MJO life cycle. A similar vertical progression of increased moisture and warmth from the boundary layer to the tropopause during deep convective development is seen in the model and observations. The magnitude, timing, and vertical structure of westerly wind onset as well as the magnitude and timing of maximum westerlies following intense convection are well simulated. In both the SP-CAM and reanalysis, there is evidence of low-level convective heating preceding deep convective heating. Meridional convergence within the boundary layer leads deep-layer zonal convergence and intense rainfall in the model and in nature. Additionally, the simulated horizontal advective drying that works to reduce q immediately following the heaviest rains matches the corresponding drying structure in ERA-40.

Several deficiencies of the SP-CAM are apparent from our analysis as well. Many of these biases stem from the overestimation of convective intensity for MJO disturbances with maximum rainfall centers in the west Pacific region. Such an overestimation of MJO variability was initially noted in KDR08 and is confirmed here in greater detail. In the Indian Ocean and Maritime Continent sectors, MJO structural and intensity biases are generally smaller. Compared to observations, the simulated atmosphere at the time of maximum rainfall involves more robust boundary layer cold pools; stronger vertical motion; a warmer, moister middle troposphere; greater convective heating; and less OLR. We hypothesize that several factors contribute to the overestimated MJO

convective intensity in the west Pacific, including unrealistic boundary layer interactions, the lack of weakening of simulated MJO disturbances over the Maritime Continent, and differences in the boreal winter mean state.

Implementation of a more sophisticated coupling between the atmosphere and ocean surface is the subject of current research and will lead to a more accurate depiction of surface energy exchanges, which, as we have seen in this study, have a critical impact on a broad range of space–time scales. We are hopeful that future SP-CAM simulations in which the atmosphere and ocean are more realistically coupled will show further improvement.

Acknowledgments. We thank two anonymous reviewers for their helpful comments. We also thank Marat Khairoutdinov for providing the SP-CAM data. This work has been supported by the National Science Foundation Science and Technology Center for Multi-Scale Modeling of Atmospheric Processes (CMMAP), managed by Colorado State University under cooperative agreement ATM-0425247. Additional funding came from NASA contract NNG04GI25G.

APPENDIX

Coupling between the CRM and GCM

Although all results from the SP-CAM simulation shown in this paper involve variables that are averaged to the GCM spatial scale, mutual interactions between the subgrid-scale processes captured by the CRM and the large-scale environment of the GCM play a critical role. It is useful, therefore, to outline mathematically the coupling between the host GCM and the CRM.

In stepping from time n to $n + 1$, a provisional value of the GCM variable is first computed as

$$\tilde{q}_G^{n+1} = q_G^n + B_G \Delta t_{LS}. \tag{A1}$$

Here, subscript G denotes GCM variables, Δt_{LS} is the GCM time step, q_G represents any prognostic variable except precipitating water, and B involves all large-scale, non-CRM effects (mainly advection). The CRM variables are updated using CRM advection, CRM physics, and a relaxation term involving $\tilde{q}^{n+1}$ as obtained from (A1):

$$\frac{q_C^{m+1} - q_C^m}{\Delta t_{\mathrm{CRM}}} = B_C + S_C + \left(\frac{\tilde{q}_G^{n+1} - \langle q_C^0 \rangle}{\Delta t_{LS}}\right). \tag{A2}$$

In (A2), subscript C denotes CRM variables, Δt_{CRM} is the CRM time step, S is the source/sink term, and $\langle \cdot \rangle$ denotes a CRM-domain average. It is important to note here that the CRM is not reinitialized on each GCM time step. Rather, the CRM time stepping involves a continuous series of subcycles, integrations that take place *within* each GCM time step, from $m = 0$ to $m = M$. The CRM field at the end of subcycle α is identical to the CRM field at the beginning of subcycle $\alpha + 1$, such that $(q_C^M)_\alpha = (q_C^0)_{\alpha+1}$. The GCM's only influence on the CRM is through the relaxation term in (A2), updated at each GCM time step. GCM variables are then updated according to

$$\frac{q_G^{n+1} - q_G^n}{\Delta t_{LS}} = B_G + \left(\frac{\langle q_C^{n+1} \rangle - \tilde{q}_G^{n+1}}{\Delta t_{LS}}\right), \tag{A3}$$

where the second term on the rhs of (A3) represents the influence of the CRM on the GCM.

REFERENCES

Adler, R. F., and Coauthors, 2003: The version-2 Global Precipitation Climatology Project (GPCP) monthly precipitation analysis (1979–present). *J. Hydrometeor.,* **4,** 1147–1167.

Arakawa, A., 2004: The cumulus parameterization problem: Past, present, and future. *J. Climate,* **17,** 2493–2525.

Benedict, J. J., and D. A. Randall, 2007: Observed characteristics of the MJO relative to maximum rainfall. *J. Atmos. Sci.,* **64,** 2332–2354.

Collins, W. D., and Coauthors, 2006: The formulation and atmospheric simulation of the Community Atmosphere Model version 3 (CAM3). *J. Climate,* **19,** 2144–2161.

ECMWF, cited 2003: IFS documentation CY28r1—Part IV: Physical processes. ECMWF, 175 pp. [Available online at http://www.ecmwf.int/research/ifsdocs/.]

Emanuel, K. A., 1987: An air–sea interaction model of intraseasonal oscillations in the tropics. *J. Atmos. Sci.,* **44,** 2324–2340.

Gates, W. L., 1992: AMIP: The Atmospheric Model Intercomparison Project. *Bull. Amer. Meteor. Soc.,* **73,** 1962–1970.

Grabowski, W. W., 2001: Coupling cloud processes with the large-scale dynamics using the Cloud-Resolving Convection Parameterization (CRCP). *J. Atmos. Sci.,* **58,** 978–997.

——, and P. K. Smolarkiewicz, 1999: CRCP: A cloud resolving convective parameterization for modeling the tropical convective atmosphere. *Physica D,* **133,** 171–178.

Hayashi, Y., 1979: A generalized method of resolving transient disturbances into standing and traveling waves by space–time spectral analysis. *J. Atmos. Sci.,* **36,** 1017–1029.

Hendon, H. H., and J. Glick, 1997: Intraseasonal air–sea interaction in the tropical Indian and Pacific Oceans. *J. Climate,* **10,** 647–661.

Houze, R. A., 1982: Cloud clusters and large-scale vertical motions in the tropics. *J. Meteor. Soc. Japan,* **60,** 396–409.

Hurrell, J. W., J. J. Hack, D. Shea, J. M. Caron, and J. Rosinski, 2008: A new sea surface temperature and sea ice boundary dataset for the Community Atmosphere Model. *J. Climate,* **21,** 5145–5153.

Inness, P. M., and J. M. Slingo, 2006: The interaction of the Madden–Julian oscillation and the Maritime Continent in a GCM. *Quart. J. Roy. Meteor. Soc.,* **132,** 1645–1667.

Jones, C., and B. C. Weare, 1996: The role of low-level moisture convergence and ocean latent heat fluxes in the Madden and Julian oscillation: An observational analysis using ISCCP data and ECMWF analyses. *J. Climate,* **9,** 3086–3104.

——, L. M. V. Carvalho, R. W. Higgins, D. E. Waliser, and J. K. E. Schemm, 2004: Climatology of tropical intraseasonal convective anomalies: 1979–2002. *J. Climate,* **17,** 523–539.

Kemball-Cook, S. R., and B. C. Weare, 2001: The onset of convection in the Madden–Julian oscillation. *J. Climate,* **14,** 780–793.

Khairoutdinov, M. F., and D. A. Randall, 2001: A cloud resolving model as a cloud parameterization in the NCAR Community Climate System Model: Preliminary results. *Geophys. Res. Lett.,* **28,** 3617–3620.

——, and ——, 2003: Cloud resolving modeling of the ARM summer 1997 IOP: Model formulation, results, uncertainties, and sensitivities. *J. Atmos. Sci.,* **60,** 607–625.

——, ——, and C. DeMott, 2005: Simulations of the atmospheric general circulation using a cloud-resolving model as a superparameterization of physical processes. *J. Atmos. Sci.,* **62,** 2136–2154.

——, C. DeMott, and D. Randall, 2008: Evaluation of the simulated interannual and subseasonal variability in an AMIP-style simulation using the CSU multiscale modeling framework. *J. Climate,* **21,** 413–431.

Kiladis, G. N., K. H. Straub, and P. T. Haertel, 2005: Zonal and vertical structure of the Madden–Julian oscillation. *J. Atmos. Sci.,* **62,** 2790–2809.

Kim, D., and Coauthors, 2009: Application of MJO simulation diagnostics to climate models. *J. Climate,* in press.

Lin, J., B. Mapes, M. Zhang, and M. Newman, 2004: Stratiform precipitation, vertical heating profiles, and the Madden–Julian oscillation. *J. Atmos. Sci.,* **61,** 296–309.

——, and Coauthors, 2006: Tropical intraseasonal variability in 14 IPCC AR4 Climate models. Part I: Convective signals. *J. Climate,* **19,** 2665–2690.

Lin, X., and R. H. Johnson, 1996: Kinematic and thermodynamic characteristics of the flow over the western Pacific warm pool during TOGA COARE. *J. Atmos. Sci.,* **53,** 695–715.

Luo, Z., and G. L. Stephens, 2006: An enhanced convection–wind–evaporation feedback in a superparameterization GCM (SP-GCM) depiction of the Asian summer monsoon. *Geophys. Res. Lett.,* **33,** L06707, doi:10.1029/2005GL025060.

Madden, R. A., and P. R. Julian, 1971: Detection of a 40–50-day oscillation in the zonal wind in the tropical Pacific. *J. Atmos. Sci.,* **28,** 702–708.

——, and ——, 2005: Historical perspective. *Intraseasonal Variability in the Atmospheric–Ocean Climate System,* K. M. Lau and D. E. Waliser, Eds., Springer, 1–18.

Maloney, E. D., and D. L. Hartmann, 1998: Frictional moisture convergence in a composite life cycle of the Madden–Julian oscillation. *J. Climate,* **11,** 2387–2403.

——, and A. H. Sobel, 2004: Surface fluxes and ocean coupling in the tropical intraseasonal oscillation. *J. Climate,* **17,** 4368–4386.

Miura, H., M. Satoh, T. Nasuno, A. T. Noda, and K. Oouchi, 2007: A Madden–Julian oscillation event realistically simulated by a global cloud-resolving model. *Science,* **318,** 1763–1765.

Myers, D. S., and D. E. Waliser, 2003: Three-dimensional water vapor and cloud variations associated with the Madden–Julian oscillation during Northern Hemisphere winter. *J. Climate,* **16,** 929–950.

Neelin, J. D., I. M. Held, and K. H. Cook, 1987: Evaporation–wind feedback and low-frequency variability in the tropical atmosphere. *J. Atmos. Sci.,* **44,** 2341–2348.

Randall, D., M. Khairoutdinov, A. Arakawa, and W. Grabowski, 2003: Breaking the cloud parameterization deadlock. *Bull. Amer. Meteor. Soc.,* **84,** 1547–1564.

Randel, D. L., T. J. Greenwald, T. H. Vonder Haar, G. L. Stephens, M. A. Ringerud, and C. L. Combs, 1996: A new global water vapor dataset. *Bull. Amer. Meteor. Soc.,* **77,** 1233–1246.

Raymond, D. J., 1995: Regulation of moist convection over the west Pacific warm pool. *J. Atmos. Sci.,* **52,** 3945–3959.

Reynolds, R. W., N. A. Rayner, T. M. Smith, D. C. Stokes, and W. Wang, 2002: An improved in situ and satellite SST analysis for climate. *J. Climate,* **15,** 1609–1625.

Salby, M. L., R. R. Garcia, and H. H. Hendon, 1994: Planetary-scale circulations in the presence of climatological and wave-induced heating. *J. Atmos. Sci.,* **51,** 2344–2367.

Slingo, J. M., and Coauthors, 1996: Intraseasonal oscillations in 15 atmosphere general circulation models: Results from an AMIP diagnostic subproject. *Climate Dyn.,* **12,** 325–357.

Sperber, K. R., 2003: Propagation and the vertical structure of the Madden–Julian oscillation. *Mon. Wea. Rev.,* **131,** 3018–3037.

Straub, K. H., and G. N. Kiladis, 2003: The observed structure of convectively coupled Kelvin waves: Comparison with simple models of coupled wave instability. *J. Atmos. Sci.,* **60,** 1655–1668.

Thayer-Calder, K., and D. A. Randall, 2009: The role of convective moistening in the Madden–Julian oscillation. *J. Atmos. Sci.,* **66,** 3297–3312.

Uppala, S. M., and Coauthors, 2005: The ERA-40 Re-Analysis. *Quart. J. Roy. Meteor. Soc.,* **131,** 2961–3012.

Wang, B., 1988: Dynamics of tropical low-frequency waves: An analysis of the moist Kelvin wave. *J. Atmos. Sci.,* **45,** 2051–2065.

Wang, Y., W.-K. Tao, and J. Simpson, 1996: The impact of ocean surface fluxes on a TOGA COARE convective system. *Mon. Wea. Rev.,* **124,** 2753–2763.

Wheeler, M., and G. N. Kiladis, 1999: Convectively coupled equatorial waves: Analysis of clouds and temperature in the wavenumber–frequency domain. *J. Atmos. Sci.,* **56,** 374–399.

Woolnough, S. J., J. M. Slingo, and B. J. Hoskins, 2000: The relationship between convection and sea surface temperature on intraseasonal timescales. *J. Climate,* **13,** 2086–2104.

Zhang, C., 2005: Madden–Julian Oscillation. *Rev. Geophys.,* **43,** RG2003, doi:10.1029/2004RG000158.

——, and M. J. McPhaden, 2000: Intraseasonal surface cooling in the equatorial western Pacific. *J. Climate,* **13,** 2261–2276.

——, M. Dong, S. Gualdi, H. H. Hendon, E. D. Maloney, A. Marshall, K. Sperber, and W. Wang, 2006: Simulations of the Madden–Julian oscillation in four pairs of coupled and uncoupled global models. *Climate Dyn.,* **27,** 573–592, doi:10.1007/s00382-006-0148-2.

Zhang, M., 1996: Impact of convection–wind–evaporation feedback on surface climate simulation in general circulation models. *Climate Dyn.,* **12,** 299–312.

Zhang, Y., W. B. Rossow, A. A. Lacis, V. Oinas, and M. I. Mishchenko, 2004: Calculation of radiative fluxes from the surface to top of atmosphere based on ISCCP and other global data sets: Refinements of the radiative transfer model and the input data. *J. Geophys. Res.,* **109,** D19105, doi:10.1029/2003JD004457.

Zheng, Y., D. E. Waliser, W. F. Stern, and C. Jones, 2004: The role of coupled sea surface temperatures in the simulation of the tropical intraseasonal oscillation. *J. Climate,* **17,** 4109–4134.

Zhu, H., H. Hendon, and C. Jakob, 2009: Convection in a parameterized and superparameterized model and its role in the representation of the MJO. *J. Atmos. Sci.,* **66,** 2796–2811.

Zipser, E. J., 1969: The role of organized unsaturated convective downdrafts in the structure and rapid decay of an equatorial disturbance. *J. Appl. Meteor.,* **8,** 799–814.